The Dissertation Committee for Xuejian Ma
certifies that this is the approved version of the following dissertation:

Spatio-Temporal-Spectral Imaging of Photo-carrier Dynamics in Perovskites and Two-dimensional Semiconductors

Committee:

Keji Lai, Supervisor

Xiaoqin (Elaine) Li

Alexander A Demkov

Linda E. Reichl

Yuebing Zheng

Spatio-Temporal-Spectral Imaging of Photo-carrier Dynamics in Perovskites and Two-dimensional Semiconductors

by

Xuejian Ma

Dissertation

Presented to the Faculty of the Graduate School of
The University of Texas at Austin
in Partial Fulfillment
of the Requirements
for the Degree of

Doctor of Philosophy

The University of Texas at Austin
August 2023

Dedicated to my beloved parents.

Acknowledgments

I am deeply grateful for the guidance, mentorship, and unwavering support of my esteemed PhD supervisor, Prof. Keji Lai. His exceptional degree of patience and profound knowledge has been invaluable to me throughout my journey to earning my doctoral degree. I am especially grateful for his willingness to foster open communication about difficulties and obstacles, offering sound advice that has helped me in times of hardship and despair. His influence will forever remain as a beacon in the voyage of my life.

In addition, I wish to extend my heartfelt gratitude to my labmates. A particular note of thanks to Dr Zhaodong Chu, whose efforts made laser-illuminated MIM a reality in our lab, thereby achieving significant strides in the field of 2D physics and beyond. His mentorship, always demonstrated with immense patience, has enriched my understanding of both basic and advanced MIM techniques as well as optical skills. I am also indebted to Dr Xiaoyu Wu, Dr Di Wu, and Dr Lu Zheng, who, through their tireless efforts and time commitment, laid a robust foundation for our lab, setting the stage for all subsequent experiments, including my own.

Furthermore, I would like to convey my appreciation to David Wannlund, Jia Yu, Alex Stram, Parth H Dave, Shaopeng Feng, Dishan Abeysinghe, and Aravind Karthigeyan. My collaborations with them on optical MIM instrumentation, measurements, and material exfoliation have been truly enriching. I am equally thankful to Dr Di Wu, Dr Zhanzhi Jiang, Dr Ashish Gangshettiwar, Dr Hongtao Yan, Daehun Lee, Shizai Chu, Xiaoru Zhang, Shahin Jahanbani, and Zifan Xu. The discussions I've had with them about research and projects have been highly insightful and educative.

I would like to acknowledge my collaborators as well. Without their contribution and support, the achievements I have made during my doctoral years would not have been possible. I extend special thanks to Prof. Xiaoqin (Elaine) Li and her students Dr Jiamin Quan, Dr Di Huang, Yue Ni, and Zhida Liu. Their constant support, both in terms of instruments and coordination, coupled with their invaluable advice over the years, has been instrumental to my progress. Prof. Kai Zhu and his student Dr Fei Zhang from the National Renewable Energy Laboratory deserve my sincere gratitude for providing state-of-the-art perovskite samples and conducting optical measurements. Equally, I am thankful to Prof. Yuebing Zheng and his students Dr Kan Yao and Anand Swain for generously providing access to their high-end laser equipment, which greatly aided in our MIM spectroscopy system development.

I want to express my profound gratitude to Prof. Xiaoqin (Elaine) Li, Prof. Alexander A Demkov, Prof. Linda E. Reichl, Prof. Yuebing Zheng, and Prof. Keji Lai for their invaluable participation in my Ph.D. dissertation committee.

Finally, I cannot express enough gratitude to my family - my cherished grandmother, Chunming Hao, and my beloved parents, Yutao Ma and Daiying Ma. Their unwavering love and faith in me, as well as their undying support for the decisions I make, cannot be overstated.

Abstract

Spatio-Temporal-Spectral Imaging of Photo-carrier Dynamics in Perovskites and Two-dimensional Semiconductors

Xuejian Ma, PhD
The University of Texas at Austin, 2023

Supervisor: Keji Lai

Laser-illuminated microwave impedance microscopy (iMIM) is a scanning probe microscopy technique that measures the spatiotemporal and spectral responses of photo-carriers in materials under laser illumination. In this dissertation, we use iMIM to study the photo-carrier dynamics in perovskites and two-dimensional (2D) semiconductors, which are promising materials for optoelectronic applications. We investigate the effects of laser power, wavelength, and sample temperature on the iMIM signals, and we reveal the underlying mechanisms of photo-carrier generation, transport, and recombination in these materials. We also demonstrate the potential of iMIM for imaging the spatial distribution of defects, grain boundaries, and heterostructures in perovskites and 2D semiconductors. Our results provide new insights into the photophysical properties of these materials and pave the way for their optimization and integration in future devices.

In this dissertation, I introduce the background and motivation of studying

perovskites and 2D semiconductors using iMIM in Chapter 1. In Chapter 2, I explain the basic principles and finite-element analysis of microwave impedance microscopy (MIM). In Chapter 3, I describe the optical MIM systems that I have contributed to or led their development, including systems for photoconductivity mapping, carrier diffusion measurement, time-resolved iMIM, and iMIM spectroscopy. In Chapter 4, I present the paper that utilized the illuminated MIM systems to reveal the dynamics of photo-carriers in organic-inorganic perovskites. I show how defects and varying types of carriers influence the optoelectronic properties of perovskite solar cells on a microscopic scale. In Chapter 5, I illustrate how our innovatively designed iMIM spectroscopy equipment can effectively reveal the exciton properties inherent in monolayer transition metal dichalcogenides (TMDs), with a special focus on WS_2 and WSe_2. I discuss how exciton binding energy, lifetime, and density depend on laser wavelength. In Chapter 6, I summarize the main findings and contributions of this dissertation and provide some outlooks for future research directions.

Table of Contents

List of Figures

Chapter 1: Introduction

The aspiration to unravel the microscopic properties of materials has been a long-standing pursuit. Equipped with proper toolkits, we are able to delve deeper into the intricate world at the microscale. This pursuit has led to the development of various tools, each with its unique capabilities and applications. Among these, Microwave Impedance Microscopy (MIM) stands out due to its distinctive ability to display local admittance properties of a sample non-invasively, providing a detailed view of the material's microscopic features.

One of the intriguing aspects that MIM can investigate is the dynamics of photogenerated carriers. This is a critical area of study as it provides insights into the behavior of charge carriers when exposed to light, which is fundamental in many fields such as photovoltaics and optoelectronics. Our existing laser-illuminated MIM (iMIM) spatial scanning has been instrumental in this regard, but the journey towards advancing this technology did not stop there.

It was a rewarding experience to contribute to the evolution of iMIM by incorporating both temporal and spectral dimensions into the picture. Those advancements have significantly broadened the scope of MIM, allowing for a more comprehensive analysis of materials at the microscopic level.

In recent years, there has been a surge in research focusing on organic-inorganic perovskites and semiconducting transition metal dichalcogenide (TMD) materials. These materials have shown promising properties for various applications from electronics to energy production. The enhanced iMIM tool is particularly beneficial in these fields, with its ability to provide high-resolution images of local conductance,

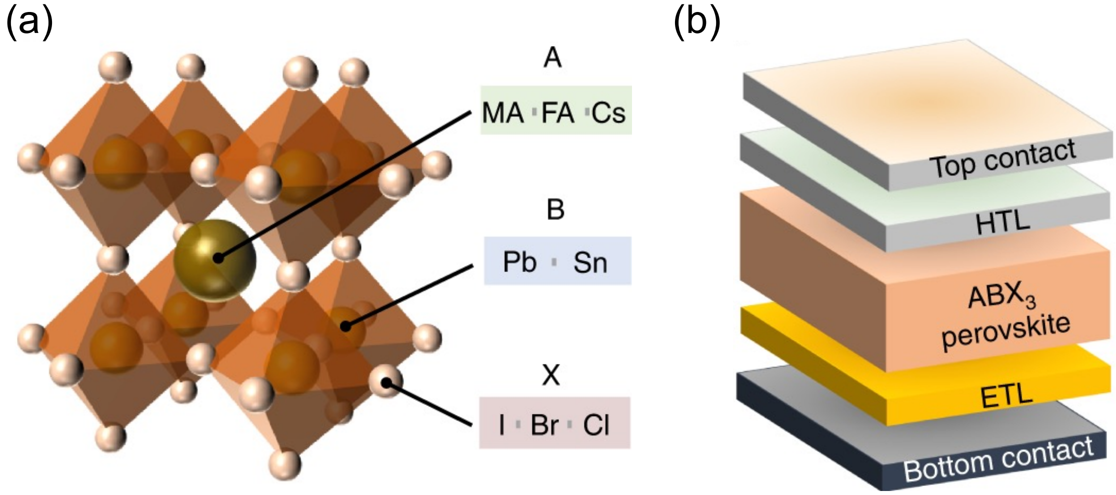

Figure 1.1: (a) Schematic structure of the MHP semiconductor family (chemical formula, ABX_3) most typically implemented in PSCs. (b) Schematics showing the layer-by-layer device structure of a typical PSC. Panel a, b and the captions are adapted with permission from Ref. [1].

carrier lifetime dynamics, and spectral excitonic behaviors, which is unique and crucial for understanding both the electronic and optical properties of these materials in a non-invasive manner.

1.1 Organic-inorganic Perovskites

Perovskite solar cells (PSCs) have emerged as a revolutionary technology in the realm of photovoltaics, demonstrating extraordinary optical and electrical properties that distinguish them from other existing photovoltaic materials. Organic-inorganic lead trihalide perovskites, a type of perovskite, have become a focal point in the field due to their extraordinary performance in solar cells. Over the past decade, the efficiency of PSCs has seen a rapid increase from 3.8% to over 25%, making them a compelling area of research for both academic and industrial sectors. [5, 6] Those PSCs are typically composed of metal halide perovskites with the chemical structure ABX3, where 'A' is a monovalent cation such as methylammonium (MA), formamidinium (FA), or cesium (Cs), 'B' is a metal ion like Pb or Sn, and 'X' is a halide ion like I^-, Br^-, or Cl^-, as shown in Figure 1.1(a). [6]

The unprecedented increase in the power conversion efficiencies (PCEs) of PSCs has been driven by their unique material properties including high absorption coefficients, low exciton binding energy, bandgap tunability, ambipolar transport characteristics, and long charge-carrier lifetimes, among others. [6] These characteristics are testament to the robust photo-physical properties of PSCs and underline their potential in photovoltaic applications where both electrons and holes are active in the photoconduction process.

Typical structure of PSCs involves a transparent conductive oxide, an electron transporting layer, a perovskite absorption layer, a hole transporting layer, and a counter electrode. [6] The operation of these cells is relatively straightforward; upon light absorption, electron-hole pairs are generated in the perovskite layer and are then extracted through the charge-selective hole and electron transporting materials to the corresponding conductive electrodes, as shown in Figure 1.1(b). [6]

One of the major advantages of PSCs, is their cost-effectiveness and simplicity of fabrication compared to other types of solar cells. Unlike silicon solar cells, which require pure silicon produced by heating sand at high temperatures and complicated manufacturing processes, perovskite materials can be solution-processed, significantly reducing the energy and cost of production. [6]

The promise of PSCs extends beyond traditional photovoltaic applications. Motivated by the significant advancements in PCEs, researchers are now beginning to explore the use of PSCs as an energy source for integrated systems such as energy conversion and storage devices, unlocking a wide range of potential applications. [6]

Despite the challenges that still need to be addressed, including stability issues and the environmentally impactful presence of lead in these perovskites, the future of PSCs in photovoltaic research and applications appears bright. [5] The rapid progress and the possibilities that they hold for the future of sustainable energy make perovskites, and more specifically organic-inorganic lead trihalide perovskites, an exciting frontier in photovoltaic research.

iMIM can be extremely beneficial in perovskite research as it provides high-resolution spatial mapping of the local photovoltaic response, enabling the study of charge transport and recombination processes in perovskite solar cells on a microscopic scale. Furthermore, it offers the potential to probe the dynamic processes under light illumination, yielding insights into the operational mechanisms and performance limitations of perovskite solar cells, thus guiding the design of more efficient devices.

1.2 Semiconducting Transition Metal Dichalcogenides

Semiconducting TMD materials are transition metal dichalcogenides of the type MX_2, where M is a transition metal (i.e. Mo, W) and X is a chalcogen (i.e. S, Se). They have a layered structure with a hexagonal plane of metal atoms sandwiched between two planes of chalcogen atoms. Four typical family members WS_2, WSe_2, MoS_2, and $MoSe_2$ have trigonal prismatic coordination. [7–10], as shown in Figure 1.2(a).

TMD monolayers are atomically thin semiconductors that can be obtained by exfoliating bulk TMD crystals or by other methods such as chemical vapor deposition, molecular beam epitaxy (MBE). TMD monolayers have properties that are distinctly different from those of the bulk crystals or other 2D materials such as graphene, which

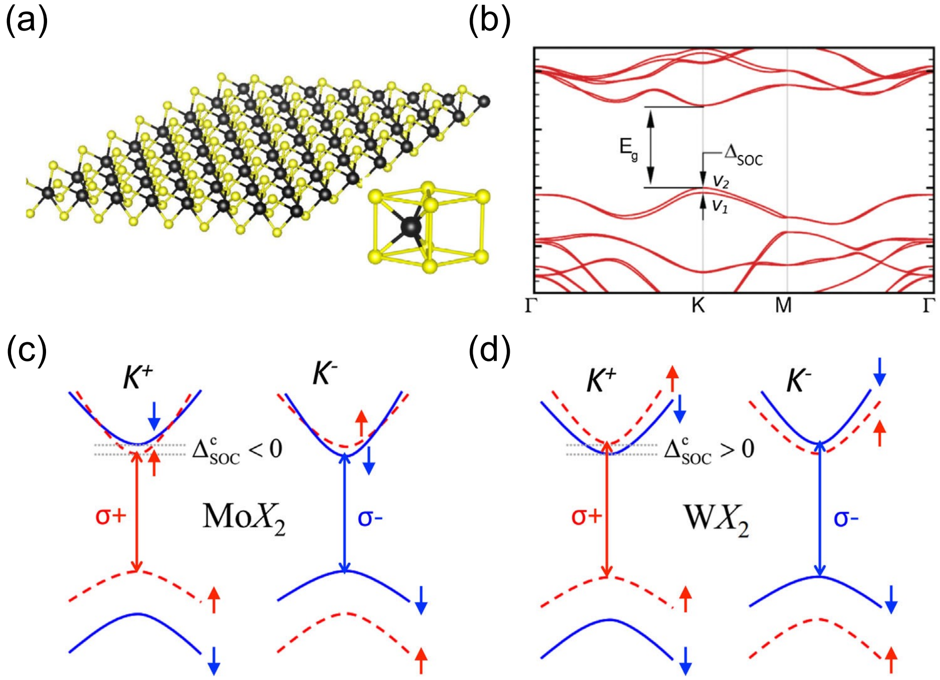

Figure 1.2: (a) Monolayer transition metal dichalcogenide crystal structure. The transition metal atoms appear in black, the chalcogen atoms in yellow. (b) Typical band structure for MX_2 monolayers calculated using density functional theory and showing the quasiparticle band gap E_g at the K points and the spin-orbit splitting in the valence band. (c), (d) Schematic illustrations in a single-particle picture show that the order of the conduction bands is opposite in MoX_2 (c) and WX_2 (d) monolayers. The contribution from Coulomb-exchange effects that has to be added to calculate the separation between optically active (bright—spin-allowed) and optically inactive (dark—spin-forbidden) excitons is not shown. Panel a-d and the captions are adapted with permission from Ref. [2].

has a gapless Dirac cone band structure as a semimetal. [11] For example, group-VI TMD monolayers (such as MoS_2, WS_2, $MoSe_2$, and WSe_2) exhibit a direct bandgap in the range of 1–2 eV, as shown in Figure 1.2(b), which can be tuned by strain, electric field, or doping. [2, 12, 13] TMD monolayers also have no inversion center, which allows them to access a new degree of freedom of charge carriers, namely the k-valley index, and to open up a new field of physics: valleytronics. [14–16] Moreover, TMD monolayers have a strong spin–orbit coupling, which leads to a spin–orbit splitting of hundreds meV in the valence band and a few meV in the conduction band, which allows control of the electron spin by tuning the excitation laser photon energy and handedness. [17]

Moreover, excitons, which are bound pairs of electrons and holes, play a significant role in the optical responses of these two-dimensional (2D) materials. In monolayer TMDs, the excitons exhibit remarkably strong binding energies due to reduced dielectric screening in the 2D limit, which leads to the prevalence of excitonic effects even at room temperature. [2] This contrasts with conventional 3D semiconductors, where excitonic effects are typically observable only at low temperatures. Monolayer TMDs can host various types of excitons, including neutral excitons, trions (charged excitons), and biexcitons, each with distinct properties and dynamics. [2] Understanding the physics of these excitons is vital for harnessing the full potential of TMDs in device applications.

Overall, TMD monolayers endowed with distinctive optical, electrical, and excitonic properties, hold great potential for advancements in fields like electronics, optoelectronics, spintronics, photonics, and quantum devices. Furthermore, their ability to form homobilayers or heterostructures opens up avenues for the exploration of novel physical phenomena, such as the intriguing moiré superlattices. [18–20] iMIM, with its high resolution and unique ability to reveal the intricate details of electronic, optical, and excitonic behaviors under light illumination, empowers researchers to better understand, optimize, and harness these materials for next-generation applications.

1.3 Dissertation Outline

In this dissertation, I will present the optical MIM systems that I have had the privilege to participate in or lead their development. I will provide a detailed account of how our equipment has been used to study the rich properties of carrier lifetime, mobility, and excitonic physics in high-performance organic-inorganic perovskites and transition metal dichalcogenides materials (TMDs). These studies have provided valuable insights into these materials, contributing to our understanding and potentially leading to their improved performance in various applications.

In Chapter 2, I will delve into the fundamental principles underlying pristine MIM electronics and their associated simulations. Following this, Chapter 3 will focus on our optically coupled MIM systems, which I have had the privilege of contributing to or leading their design and development. This includes systems for photoconductivity mapping, carrier diffusion measurement, time-resolved MIM, and MIM spectroscopy. This chapter will offer an in-depth look at these advanced systems, highlighting their unique features, capabilities, and the role they play in our ongoing research. Chapter 4 will feature two papers that utilized the illuminated MIM systems to reveal the dynamics of photo-carriers in monolayer Transition Metal Dichalcogenides (TMDs) and organic-inorganic perovskites. This chapter will highlight how defects and various types of carriers influence the optoelectronic properties of 2D semiconductors. Finally, in Chapter 5, I will illustrate how our innovatively designed MIM spectroscopy equipment can effectively reveal the exciton properties inherent in monolayer TMD materials, with a special focus on WS_2 and WSe_2.

Chapter 2: Microwave Impedance Microscopy

In traditional optical systems, measurement resolution is typically constrained by the diffraction limit, represented by the formula $\frac{\lambda}{2N.A.}$, where λ denotes the wavelength of the illuminated electromagnetic wave, and $N.A.$ signifies the numerical aperture. This limitation makes it challenging to resolve features at nanometer scales, as it would require wavelengths shorter than ultraviolet light.

To overcome this barrier, researchers have explored alternative methods such as scanning probe microscopy (SPM). SPM employs a sharp near-field probe for signal detection, thereby enhancing resolution to the dimension of the tip apex, which can reach nanometer dimensions.

Among various SPM techniques, microwave impedance microscopy (MIM) is notable for its capacity to non-invasively detect local impedance of a sample with high precision. MIM operates by directing a microwave signal towards the sharp probe and gathering signals reflected from the tip-sample interaction region. This process enables the decoding of conductivity and permittivity information in the local area, providing a powerful tool for non-invasively obtaining micro- and meso-scopic properties across a sample.

2.1 Basic Principles

A fully operational Microwave Impedance Microscopy (MIM) system, as depicted in Figure 2.1, comprises two main components: the AFM scanning system and the MIM electronics. As a scanning probe system, MIM employs a metal tip, which can be either commercially available or custom-made, in an atomic force microscope

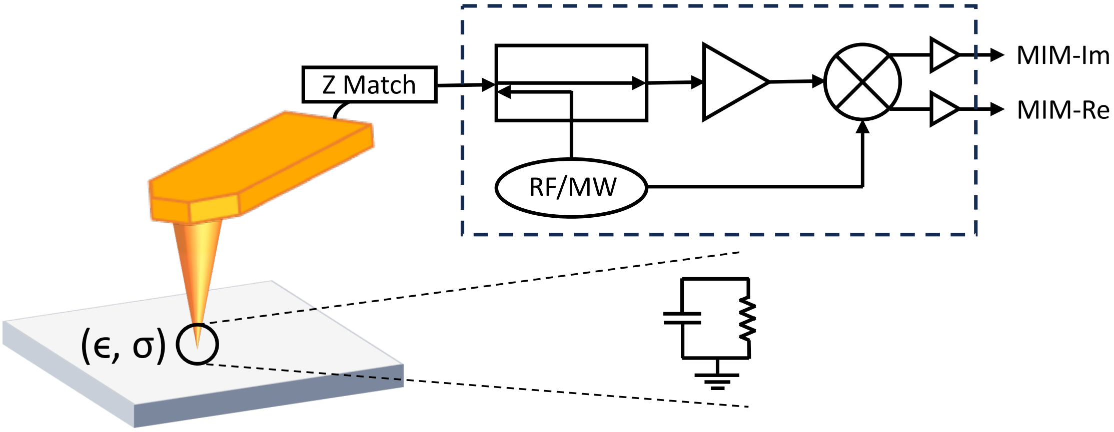

Figure 2.1: Schematic of microwave impedance microscopy

as its probe.

The MIM electronics dispatch microwave signals to the tip and subsequently collect the reflected signal from the tip-sample interaction region on a point-by-point basis. This process enables the mapping of MIM responses across a finite area, typically spanning tens of micrometers, with resolutions that can be as high as the dimension of the tip apex, usually ranging from a single nanometer to tens of nanometers.

The MIM electronics typically produce two orthogonal outputs, which correspond to the imaginary and real parts of the local admittance of the tip-sample interaction region. By decoding these imaginary and real parts through appropriate finite-element analysis, one can determine the local conductivity (σ) and permittivity (ϵ).

2.2 Scanning Probes

In our research laboratory, we frequently utilize three types of scanning probes, as illustrated in Figure 2.2.

The first type is the shielded cantilever probe from PrimeNano Inc., manu-

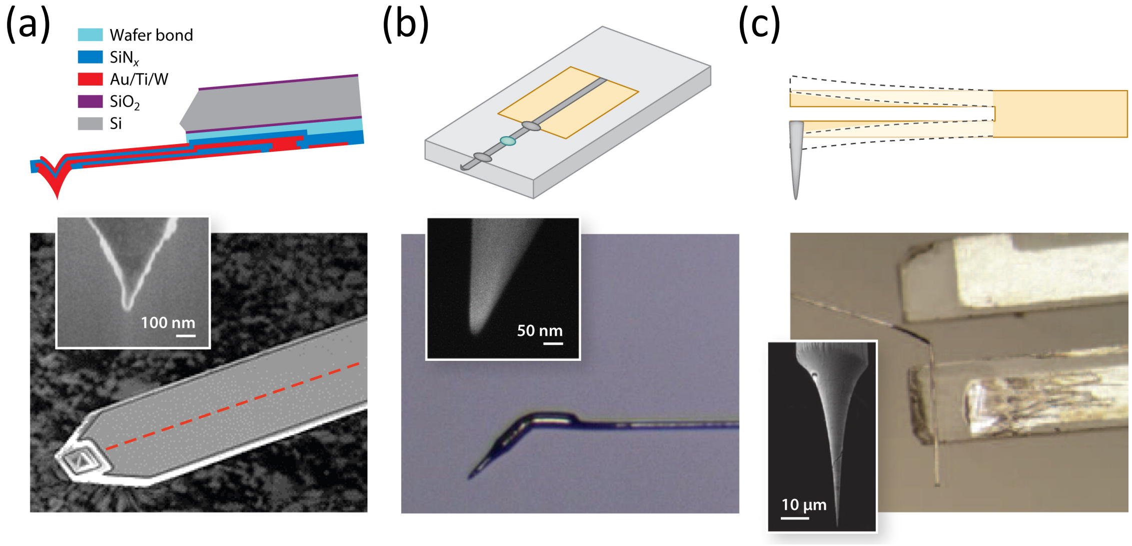

Figure 2.2: Three types of commonly used scanning probes for MIM. Upper panels are schematics and bottom panels are corresponding scanning electron micrographs. Panel a-c, and the captions are adapted with permission from Ref. [3].

factured using MEMS processes. This commercially available probe is widely used in our lab for rapid room-temperature testing, and its shielding generally ensures a satisfactory signal-to-noise ratio. The center conductor, made of Au/Ti/W and responsible for transmitting the microwave signals, is encased within SiNx layers and safeguarded by metal layers. The tip apex, which is less than 100nm in size, is crafted through an oxidation sharpening process of the sacrificial Si pit, followed by a metal refill. However, this type of tip is not extensively employed in illuminated MIM measurements, as the layered structure can introduce artifacts to the MIM signals due to thermal expansion effects from the layers, particularly affecting the imaginary part.

The second type is the Pt-only tip from Rocky Mountain Nanotechnology LLC. This tip employs a different approach to mitigate the influence of strong stray-field contribution, achieved by using a tall metal tip shank, approximately 80 µm in height. These tips are commonly used in our illuminated MIM measurements due to

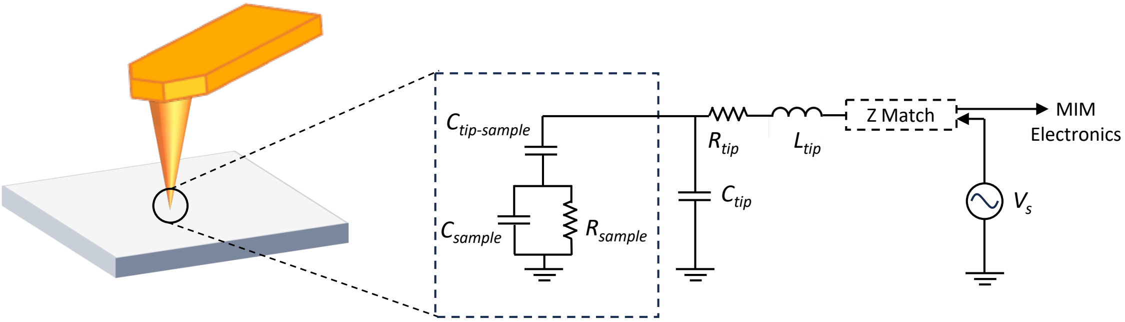

Figure 2.3: Equivalent Circuit of Tip-Sample Interaction Region

their non-layered structure and low spring constants, which are crucial for contact measurements without feedback loops.

The third type is the quartz tuning fork (TF)-based probe with home-etched metal (typically tungsten) tips. Although a TF probe is somewhat more challenging to operate compared to the other two types, it offers the ability to demodulate with its distance oscillation of about 10nm. This feature provides the absolute value of the MIM signal after subtracting the background, thereby countering the DC drift of the MIM electronics. This type of probe is preferred in certain low-temperature measurements due to its self-sensing capability, even in cryogenic environments.

2.3 Tip-sample Interaction

To interpret the signals obtained from MIM measurements, it is essential to first examine the tip-sample interaction. This microscopic interaction informs us how local properties influence MIM signals, thereby aiding our understanding of what MIM signals represent in actual experiments.

As depicted in 2.3, the tip-sample interaction region can typically be modeled as lumped elements. This modeling is feasible because the dimension of the tip-interaction region is significantly smaller than the microwave's wavelength, allowing the area to be treated as quasi-static.

The tip-sample interaction circuit can be represented as a capacitor between the tip and sample, in series with the sample resistance and capacitance in parallel. The sample resistance and capacitance (or overall impedance) are the information we aim to extract. The tip-sample capacitance is generally taken into account due to the native oxide at the tip apex or the intentional addition of a dielectric layer atop the active sample layer. The tip-sample interaction varies as we scan across the material with different electrical properties, which are recorded as the MIM signals.

We use Y_{ts} and Y_{gt} to denote the tip-sample admittance (the reciprocal of its impedance), and the ground-tip admittance, respectively. The total admittance is thus $Y_{total} = Y_{ts} + Y_{gt}$. The amount of microwave reflected is determined by the reflection coefficient, expressed as:

$$\Gamma = \frac{Y_0 - Y_{total}}{Y_0 + Y_{total}}$$

, where Y_0 is the transmission line admittance. A significant difference between Y_0 and Y_{total} can cause high reflection due to such impedance mismatch. We typically use impedance matching (embedding an extra coaxial cable or capacitor) to transform the Y_{total} to a new value $f(Y_{total})$, which is much closer to Y_0 and modifies the reflection coefficient to

$$\Gamma = \frac{Y_0 - y(Y_{total})}{Y_0 + y(Y_{total})}$$

.

With the reflection coefficient, it becomes straightforward to represent the signals MIM electronics collected from the reflected microwaves, which contain information about the electronic properties of the tip-sample interaction region:

$$\begin{aligned} MIM &= V_{in} e^{i\Phi} \Gamma \\ &= V_{in} e^{i\Phi} \frac{Y_0 - y(Y_{total})}{Y_0 + y(Y_{total})} \\ &= e^{i\Phi} f(Y_{total}) \end{aligned}$$

, where V_{in} is the incident microwave signal, Φ is the demodulation reference phase, and $f(Y_{total}) = V_{in} \frac{Y_0 - y(Y_{total})}{Y_0 + y(Y_{total})}$. The complex nature of the microwave reflection requires us to have two channels to represent MIM-Im and MIM-Re parts separately as in $MIM = MIM_{Re} + i \cdot MIM_{Im}$.

In comparison to Y_{gt}, T_{ts} typically exhibits much smaller magnitudes due to its relatively small tip-sample interaction region. Consequently, we can expand the MIM signals by considering Y_{ts} as a perturbation to Y_{total} and accordingly expand the MIM term. This can be represented as:

$$MIM \approx e^{i\Phi} f(Y_{gt}) + e^{i\Phi} f'(Y_{gt}) Y_{ts}$$

Here, f' denotes the derivative of f. Given that the admittance between the tip and ground is usually stable and can be treated as a constant, we can consider the terms with Y_{gt} as constants. This can be expressed as:

$$MIM \approx e^{i\Phi}(aY_{ts} + b)$$

In this equation, $a = f'(Y_{gt})$ and $b = f(Y_{gt})$. This expression can be further simplified by adjusting Φ to make $e^{i\Phi}$ a real number. This adjustment can be achieved through a calibration experiment that maximizes/minimizes imaginary/real parts with known reference samples. Ultimately, we obtain:

$$\begin{aligned} MIM &= MIM_{Re} + MIM_{Im} \\ &\approx a(Re(Y_{ts}) + Im(Y_{ts})) + b \end{aligned}$$

By offsetting the constant term, we establish the correspondence between the two channels of MIM signals and the admittance of the tip-sample interaction region:

$$\Delta MIM_{Re} = a \cdot Re(\Delta Y_{ts})$$

$$\Delta MIM_{Im} = a \cdot Im(\Delta Y_{ts})$$

Therefore, we establish a direct correlation between the real and imaginary components of the MIM signals and the corresponding real and imaginary parts of the admittance within the tip-sample interaction region. This relationship is fundamental to our understanding and interpretation of MIM measurements, enabling us to extract meaningful and accurate data from these signals.

2.4 MIM Electronics and Impedance Match

The MIM electronics typically comprise several key components: RF/Microwave signal generators, impedance matches, couplers, cancellation circuits, IQ mixers, and amplifiers. These components work together to facilitate the functioning of the MIM system.

RF/Microwave signal generators produce microwaves ranging from 300MHz to 300GHz, a range low enough to prevent triggering interband carrier transitions. Impedance matches are crucial to maximize the transition of the microwave from the source to the tip, minimizing loss. Couplers direct the reflected signal, while cancellation circuits compensate for the background signal. IQ mixers demodulate the reflected signals, and amplifiers boost the MIM outputs of small orders. For a more detailed understanding of the circuit design of a specific MIM box, please refer to [21].

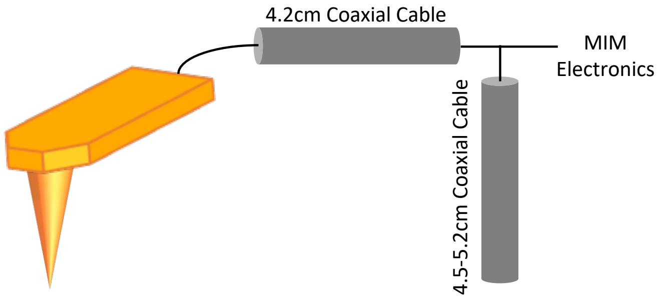

Figure 2.4: Impedance match with coaxial cables

The design of the impedance match warrants further explanation, as it may vary for different tips and measurements. As a transmission line, the MIM circuit from the source to the tip apex requires appropriate impedance matching to reduce reflection before the signal reaches the sample. Without this, there will not be sufficient reflected signal from the sample to the MIM outputs to decode the local electrical properties.

In practice, there are typically two methods to handle impedance matching. The first involves the introduction of a quarter-wave coaxial cable, as depicted in Figure 2.4. We employ wire bond techniques to connect the metal exposure of the tip cantilever with a quarter-wave coaxial cable. For a 1GHz MIM circuit, the typical length of the coaxial cable is around 4.2cm. Another open-end coaxial cable stub is connected in parallel to match the impedance of the circuit.

By adjusting (shortening) the cable stub, one can conveniently modify the impedance to an optimal value. While adjusting the stub length, we can connect this near-tip circuit to the S_{11} or S_{22} channel of a Vector Network Analyzer and monitor the dips in the spectrum. When the desired dip nears the minimum, we achieve minimal signal reflection and maximal signal transmission all the way to the

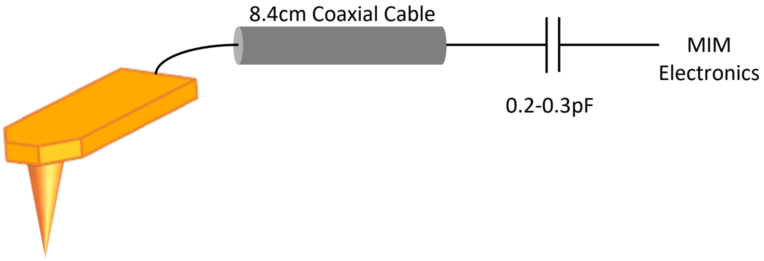

Figure 2.5: Impedance match with capacitors

tip under the dip frequency.

The second method to achieve impedance matching involves introducing capacitors connected in series to the coaxial cable, as shown in Figure 2.5. To achieve a similar effect as the cable stub, a typical capacitance of $0.2 - 0.3\mu$F is required for a 1GHz MIM circuit. Since capacitors are usually not adjustable, we do not have the flexibility to tune impedance while monitoring the VNA. However, the significantly smaller space that capacitors occupy compared to cable stubs can be essential for some constrained areas, especially in certain low-temperature cryostats.

2.5 Finite-Element Analysis

The dielectric response at a given position r within a sample can be represented as:

$$\hat{\varepsilon}(r) = \varepsilon'(r) + i[\varepsilon''(r) + \frac{\sigma(r)}{\omega}]$$

In this equation, $\varepsilon'(r)$ and $\varepsilon''(r)$ denote the real and imaginary parts of the permittivity, respectively. $\sigma(r)$ represents the conductivity, and ω is the angular frequency of the electric field. For a specific tip-sample profile, Finite-Element Analysis

(FEA) over r is needed to obtain the overall MIM signals. This process establishes the correlation between the electrical properties of the sample and the resulting MIM signals.

While the admittance extracted from MIM signals contains information about local permittivity and conductivity, our primary interest in optical studies lies in the changes in photo-conductivities. Therefore, throughout this dissertation, we will concentrate on conductivity measurements. To establish a connection between the MIM signals collected by the tip and the physical conductivities of the tip-sample interaction region, it is essential to consider the layer structures and electrical properties within the tip-sample interaction region.

It is worth noting that any alteration in the tip profile, such as enlarging the apex aperture, can significantly influence the signal levels, even when examining the same sample. Additionally, the way signals fluctuate with increasing or decreasing local conductivity due to sample changes, light illumination, or the application of gate voltages to adjust Fermi levels, is also of interest. These variations are primarily attributed to different potential and electric field distributions when the tip-sample interaction region changes for different tips and samples.

Therefore, to accurately extract quantitative conductivity values from MIM signals, it is crucial to have a well-defined Finite-Element Analysis (FEA) model. This model can simulate the response of MIM signals to changes in conductivity, providing a robust tool for interpreting signals from MIM measurements.

For optically coupled MIM measurements, we primarily utilize the commercial software Comsol Multiphysics 4.4 for simulations, focusing on tips from Rocky Mountain Nanotechnology LLC (abbreviated as RM tips) and samples such as perovskites and Transition Metal Dichalcogenides (TMDs). The RM tips are cone-shaped with

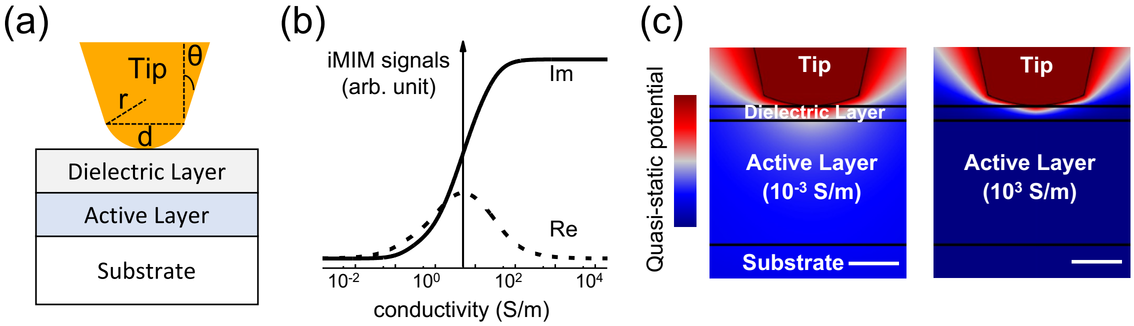

Figure 2.6: Tip-sample geometry and FEA simulation. (a) Tip-sample geometry (b) MIM response curve from FEA simulation (c) Quasi-static potential distribution of FEA simulation at $\sigma = 10^{-3}$S/m and $\sigma = 10^{3}$S/m. Panels b-c, and the captions are adapted with permission from Ref. [4].

inherent axis symmetry. Moreover, the samples examined in this dissertation typically exhibit axis-symmetry properties beyond the scale of the tip-sample interaction region. Examples include regular monolayer TMD flakes, which can span tens of micrometers, and organic-inorganic halide perovskites, which possess micrometer-level grain sizes. Consequently, we can leverage the axis-symmetry property in the simulations by employing the 2D axisymmetry mode of Comsol Multiphysics. This approach significantly reduces the simulation running time and requires input of only half of the 2D vertical cross-section surface of the tip-sample interaction region.

With this in mind, it is essential to accurately depict the geometries of the tip and the sample to ensure precise simulation results. Scanning Electron Microscopy (SEM) is typically utilized to estimate the tip shape. With the SEM image of the tip, one can conveniently construct the cross-section geometry with appropriate parameters using geometry elements of squares, triangles, and curves on Comsol, as demonstrated in the tip geometry model shown in Figure 2.6 (a). The geometry of samples can be easily obtained through regular Atomic Force Microscopy (AFM) scans. As our primary focus in this dissertation is the optical conductivity response, the permittivities of the materials required for simulations in the models can be set using their known dielectric constants.

With a well-established Comsol model, we employ the AC/DC module of the software to simulate outputs of imaginary and real channels of MIM response. One can select an appropriate mesh density depending on the relative scales of the tip and sample structures. A finer mesh grid provides more accurate results, but also requires more time to run. After sweeping the sample conductivity for the model, a typical response curve and potential distribution would resemble Figure 2.6 (b-c). The imaginary part will grow monotonically, while the real part will peak at a certain conductivity and then decrease. The point at which the real part reaches the peak, just like the entire response curve, is determined by the specific model we construct for the simulation.

With the response curve from the simulation, we can compare it with the actual data of MIM-Im and MIM-Re and inversely obtain the corresponding conductivity value by finding the nearest neighbors in the simulation to the actual MIM-Im, MIM-Re pairs. In this manner, any MIM signals we measure from experiments can be converted to the conductivities we seek to understand. By mapping out a certain area with laser illumination, we can obtain the mapping of photo-conductivity accordingly. This capability enabled us to use MIM to study the photo response and corresponding properties of 2D semiconductors quantitatively, thereby contributing to the advancement of our research in this field.

Chapter 3: Light-illuminated MIM

In this chapter, I will delve into the details of the light-illuminated microwave impedance microscopy (iMIM) setups we have established in our laboratory. It's worth noting that throughout my research and discussions, the terms iMIM, optical (or optically-coupled) MIM, and laser-MIM are used interchangeably, all denoting the same core concept.

We have successfully installed three iMIM setups in different locations: our primary laboratory, Professor Xiaoqin (Elaine) Li's laboratory, and the ECE MRSEC laboratory. The photoconductivity mapping and diffusion measurement systems in our primary lab and Prof. Li's group were primarily implemented by Dr. Zhaodong Chu. The time-resolved iMIM system in Prof Li's group was a collaborative effort between Dr. Zhaodong Chu and myself. The MIM spectroscopy system in the ECE MRSEC lab was primarily initiated by me, developed in collaboration with Alex Stram, and facilitated by the assistance of Dr. Bin Fang.

Thus far, we have successfully developed a comprehensive toolkit for iMIM capabilities. This advanced system allows for an extensive exploration of material properties across the spatial, temporal, and spectral dimensions, such as spatiotemporal dynamics of photocarriers of photosensitive materials, energy bandgap and excitons of semiconductors, and photo-induced phase transitions in TMDs and moiré systems. The research projects on which I have published papers involve all three setups. Therefore, I will provide a detailed introduction to each of these setups before we delve into the specifics of individual projects. This comprehensive understanding of our iMIM setups will provide a solid foundation for the subsequent discussions

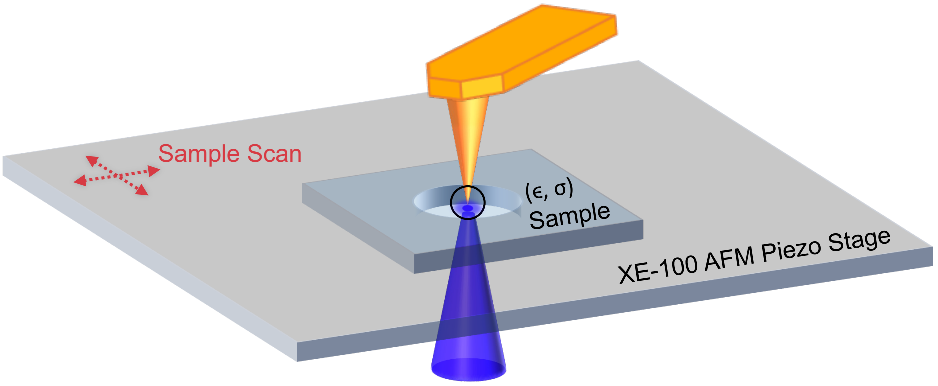

Figure 3.1: Schematic of iMIM setup for photoconductivity mapping (sample scan) based on a modified commercial XE-100 AFM system with bottom illumination. The sample moves with the piezo stage, while the tip and laser align and are fixed during scanning.

on our research findings and their implications in the field of Microwave Impedance Microscopy.

It is important to highlight that all these setups require the laser objective and tips to be positioned on opposite sides of the sample. This arrangement ensures better focus, accurate estimation of laser power, and prevents any obstruction of the laser by the cantilever, which could occur when the laser shines from the same side at a tilted angle. Consequently, the samples we examine for optical MIM are typically deposited on or transferred to transparent substrates, such as double-polished sapphire, mica, or thin glasses. This choice of substrate not only facilitates the experimental setup but also enhances the accuracy and reliability of our measurements, contributing to the overall quality of our research in Microwave Impedance Microscopy.

3.1 Photoconductivity Mapping System

The most straightforward application of iMIM is photoconductivity mapping under constant light illumination. To facilitate this, we utilize a modified XE-100 commercial Atomic Force Microscope (AFM) produced by Park Systems, which features an aperture in the piezo sample stage. This design allows us to direct the laser from the bottom to the sample while aligning the tip to the sample from the top, as depicted in Figure 3.1.

A continuous-wave (CW) laser is guided into the objective beneath the sample stage, and the laser spot is manually focused around the sample of interest. Typically, the laser spot is slightly defocused from the exact sample plane to mitigate the effect from carrier diffusion, which might decrease the concentration of free carriers under the tip aligned at the center of the laser profile, and make the tip laser alignment less error-prone.

The RM tip is visible in the camera of the XE-100 system, enabling us to conveniently align the tip and laser while monitoring their relative positions. It is also possible to use fine features on the sample surface as a more accurate reference for aligning the laser spot and tip respectively. Practically, these features can be a corner of a TMD flake or a small bubble on the surface, which should be visible in both the camera and AFM tip scanning for respective alignment of the laser spot and the tip.

During measurement, the XE100 AFM uses the cantilever-reflected laser (not the CW laser) as the feedback loop to control the tip-sample approaching process. The sample stage piezo moves the sample in x and y directions. As the CW laser spot and tip have been aligned, when the piezo scans across a certain linecut or area, the MIM signals we get from the tip will be affected by the photoconductivity under a constant laser intensity since the relative position of the laser spot and tip does not change during those scans. In this way, we can obtain the photoconductivity mapping while maintaining a constant laser intensity.

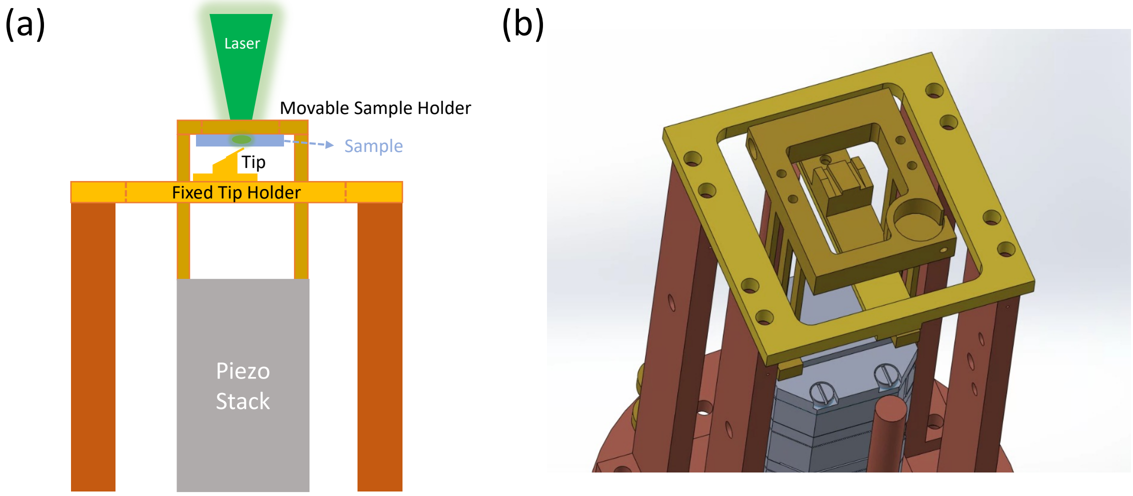

Figure 3.2: Schematic and design of photoconductivity mapping (sample scan) mode for ST500 iMIM spectroscopy system.

It is worth noting that the MIM spectroscopy system in the cryostat chamber at the EER MRSEC lab, which will be discussed in greater detail in the following sections, also supports such photoconductivity mapping mode, as shown in Figure 3.2. Low-temperature measurements are feasible in this cryostat-based system. This capability is not available with the commercial AFM, which operates exclusively at room temperature. To achieve the same sample scanning, despite having piezo stages at the bottom and lasers from the top, it requires a sophisticated sample holder and tip holder design to transfer the piezo motion at the bottom to the sample motion in the middle, while having a fixed laser from the top and a fixed tip below the movable sample holder, as illustrated in 3.2 (b).

Studies utilizing this technique will be presented in Chapter 4. This method of photoconductivity mapping under constant light illumination provides a valuable tool for investigating the photo-responsive properties of various materials, contributing to our understanding of their behavior under different conditions.

3.2 Carrier Diffusion Measurement System

By shifting the moving component from the sample holder to the tip holder, we can transform the above systems from constant illumination mapping (sample-scan mode) to carrier diffusion measurement tools (tip-scan mode). With the laser and sample held stationary, the tip, controlled by the piezo, can scan across the sample area surrounding the laser spot, thereby detecting any carrier diffusion-related MIM signals.

Such scanning is not feasible with the XE-100 commercial AFM, as its tip is fixed in the x and y directions. Similarly, moving the laser and sample simultaneously while keeping the tip stationary presents a technical challenge, especially at extremely small scales.

To overcome this limitation, we employ an ST500 cryostat system in our main lab, similar to the cryostat used for MIM spectroscopy at the ECE MRSEC lab. This system features a piezo stack at the bottom, which can hold the tip holder and move it in the z direction for approaching and in the x and y directions for scanning.

Since the use of commercial AFM's camera and approaching systems is not feasible, the diffusion measurement system relies on custom-built light illumination, camera detection, and tip approaching schematics. A comprehensive optical system was implemented, as shown in Figure 3.3.

A continuous-wave (CW) laser is focused on the sample plane by the objective, achieving the smallest profile permitted by the objective. In practice, the laser spot has a radius of 2µm. During a measurement, an optical chopper is modulating the laser intensity, outputting its chopping frequency to the lock-in amplifiers, which demodulate the signals from the MIM electronics. This demodulation process

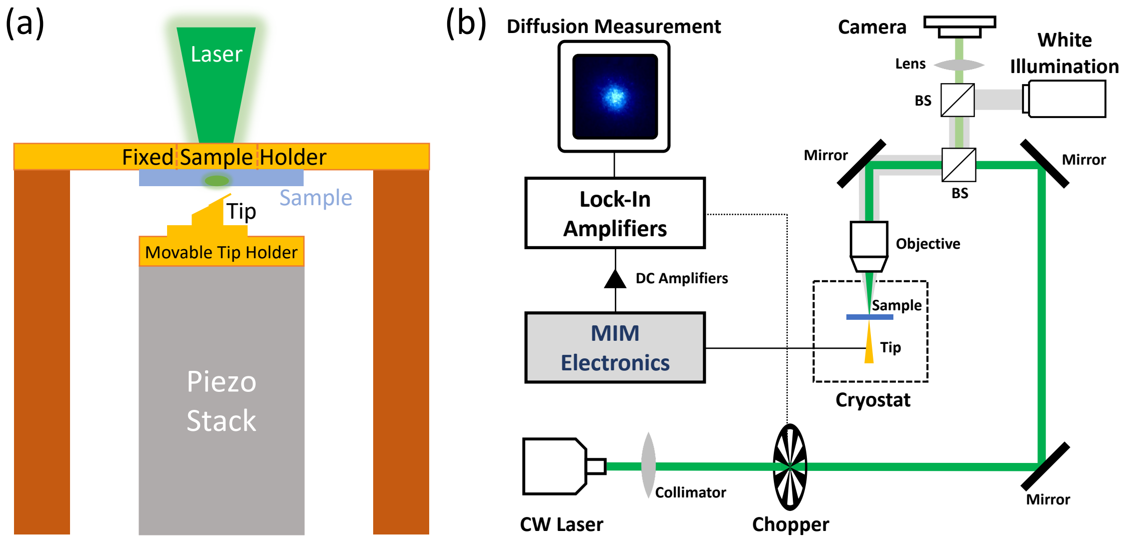

Figure 3.3: Schematic of the carrier diffusion measurement system

eliminates background signals and enhances the signal-to-noise ratio of the diffusion scans.

With appropriate time constants set on the lock-in amplifiers, the tip can scan across the sample area centered on the laser spot. The resulting system output would then reflect the carrier distributions, a combined effect of the photo-generation process and the carrier diffusion process. Intuitively, with a non-zero diffusion length, one should obtain a MIM pattern whose width is wider than the laser profile, but still centered at the laser spot. With this profile, we can use the diffusion equation convoluted with the Gaussian laser profile to quantitatively identify the diffusion length of the carriers in the sample.

In our ST500 system, we do not have a dedicated feedback loop, so we utilize an RM tip with a small spring constant (0.6 N/m). This allows the tip to scan across the samples without causing damage. The tip approaching to the sample is facilitated by applying an AC voltage to the z-scanner of the piezo stack. This action induces

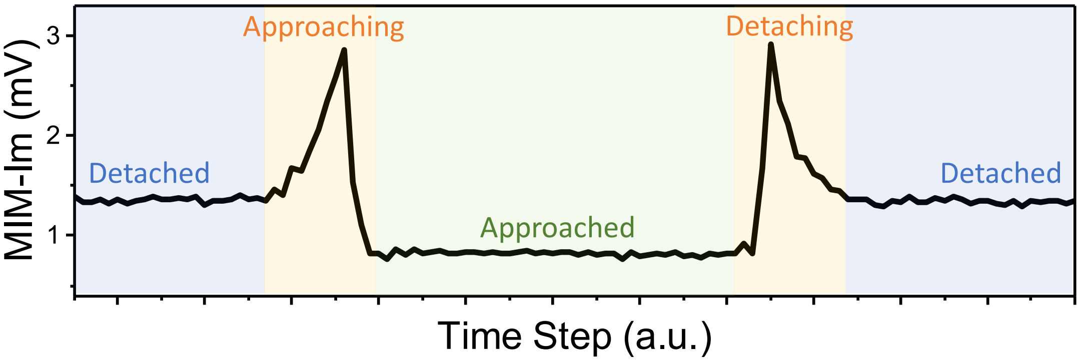

Figure 3.4: Typical approaching curve with AC demodulation in ST500.

an oscillation of the tip (along with the tip-holder), which in turn generates AC MIM signals due to the changing distance between the tip and the sample.

We prefer to use the resonance frequency of the tip holder as it produces the largest AC amplitude. These AC MIM signals can be captured by lock-in amplifiers that share the same demodulation frequency as the AC signal driving the z-scanner. By monitoring the change in the demodulated MIM signal, we can determine when the tip is approaching the sample, as the signal will increase monotonically with decreasing tip-sample distance.

A typical approaching curve looks like Figure 3.4. When the tip makes contact with the sample, the solid contact between the two changes the resonance frequency of the tip instantly. This change results in a sudden drop in the demodulated MIM signal, indicating a solid contact and thus a successful approach. The AC demodulated MIM signal also aids in distinguishing between the MIM-Im and MIM-Re parts. The oscillation of the tip around the substrate should theoretically only alter the capacitance and not the conductivity. Therefore, only the imaginary signal should capture such changes, as the real signal of an admittance corresponds only to conductivity, which should be zero and unchanging on the substrate.

A scan is then conducted with the AC signal turned off. Although the current system handles approaching, scanning, and mixer adjustment adequately, a dedicated tip approaching feedback loop would be beneficial. Such a system could be achieved by using TF tips or incorporating a cantilever-laser-based feedback loop. The former has already been used in our group for projects such as sub-10K low-temperature measurements. However, it introduces unnecessary complexity and an extra layer of demodulation for chopped-CW or pulsed laser measurements with laser-frequency demodulation. A cantilever-laser-based feedback loop is a promising direction for future enhancements to the robustness of our scans and measurements.

The same functionality of diffusion measurement was also replicated in the MIM Spectroscopy system at the ECE MRSEC lab with minor modifications. Since these systems are implemented with ST500 cryostats, they have the advantage of conducting measurements at low temperatures.

Studies utilizing the diffusion system will be discussed in Chapter 4.

3.3 Time-resolved iMIM

The Microwave Impedance Microscopy (MIM) technique with time-resolved capabilities is characterized by its ability to measure the lifetimes of free carriers generated by photon illumination. This capability is of significant importance due to the typical lifetimes of these free carriers falling within or around the nanosecond or microsecond range. Consequently, a high degree of temporal resolution is necessary for both the laser input and signal detection to facilitate accurate measurements.

The schematic of the time-resolved iMIM system (Figure 3.5) illustrates the general setup and the crucial components involved in the measurement process. Among these components, the laser source plays a vital role. The laser must be capable of rapid deactivation once it has energized and illuminated the sample.

Achieving such rapid deactivation can be accomplished through two main strategies. The first strategy involves the use of an electro-optic modulator (EOM), such as the M350-160-01 model by Conoptics Inc. This device can modulate the laser, enabling it to switch on or off within an impressively short time - as rapid as 8 nanoseconds. The modulation process is driven by TTL square waves originating from a signal generator, like the DG5071 model from RIGOL Technologies USA Inc, which boasts a rise/fall time of approximately 4 nanoseconds. This method is utilized in the XE-100 iMIM system and the ST500 system located in the main lab. Both of these systems employ the same continuous wave (CW) pigtail diodes, as outlined in the preceding section.

An alternative strategy involves replacing the CW laser with a pulsed laser. This pulsed laser possesses a rapid falling edge and a sufficiently low repetition rate, which allows the carrier concentration to decay completely before the arrival of the subsequent pulse. For instance, the ECE MRSEC lab employs the SuperK Compact Supercontinuum laser from NKT Photonics Inc, which features a pulse width of around 2 nanoseconds and a repetition rate of 20KHz, or 50 microseconds per period.

The MIM electronics used for iMIM typically operates at a frequency around 1GHz, corresponding to a period of 1 nanosecond. One of the limitations of standard MIM scanning concerning time resolution is the low-frequency amplifier, with specifications of 54 dB, 20 kHz. To uphold the 10ns MIM resolution, it is essential to replace this amplifier with a faster one, such as the SR445A by Stanford Research Systems Inc. This faster amplifier, highlighted in Figure 3.5, has specifications of 28

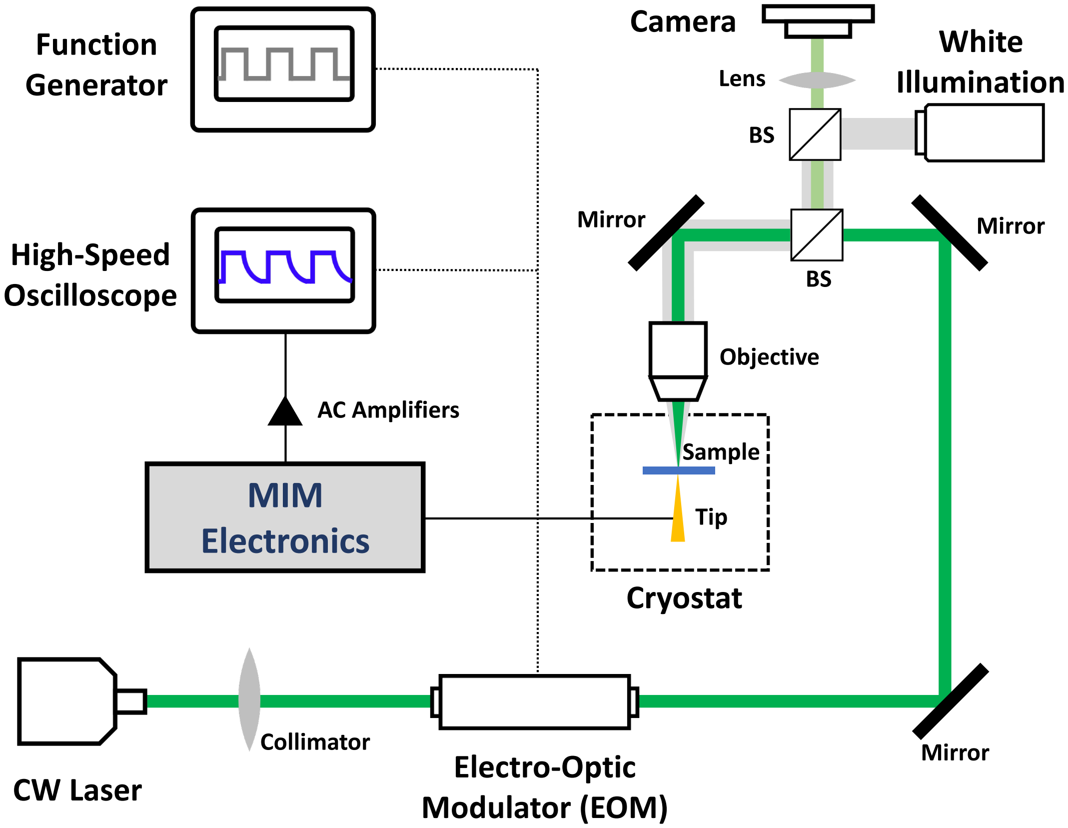

Figure 3.5: Schematic of the time-resolved iMIM system

dB, 350 MHz. However, this amplifier does not filter as many high-frequency signals or noise, leading to an inevitable reduction in the signal-to-noise ratio.

To address this issue and to obtain accurate signal readings with high resolution, we employ a fast-response oscilloscope to capture the signals and perform substantial averaging. In our labs, we use two fast-sampling oscilloscopes: the DS6062 (600MHz, 5GSa/s) and MSO8204 (2GHz, 10GSa/s), both supplied by RIGOL Technologies USA Inc.

By employing the aforementioned laser modulation and oscilloscope data collection techniques, we can achieve a temporal resolution of about 10 nanoseconds. The potential applications and more detailed exploration of time-resolved MIM will be addressed in Chapters 4 and 5.

3.4 iMIM Spectroscopy

The specialized iMIM setups as described above have already enabled us to perform a wide range of photocarrier-related measurements, elucidating the spatiotemporal dynamics of these carriers with considerable efficacy. However, in order to fully realize the potential of optical coupling in MIM measurements, there remains an essential aspect that has not yet been discussed - spectroscopy measurement.

Incorporating a capability for sweeping wavelengths could significantly broaden the range of potential research areas that could be investigated. Such a feature would allow us to delve deeper into various fields of interest, including but not limited to the exploration of energy gaps in semiconductors and the intricate physics of excitons. By adding this spectroscopy dimension to the MIM technique, we can enhance our understanding of material properties at a microscopic level, thereby opening the door to numerous possibilities for scientific discovery.

Our work requires a light source capable of continuous wavelength sweeping, for which a supercontinuum white light source would satisfy the requirement. In our systems, we have opted to utilize two laser sources from NKT Photonics Inc: the SuperK COMPACT (450-2400nm, 20kHz) and the SuperK FIANIUM (400-2400nm, 78MHz). These two laser sources are chosen primarily because they offer a broad wavelength coverage, extending to the near-visible range, which is a region of keen interest in our study. Furthermore, these two sources exhibit a difference in repetition rate. We exploit this variation to fulfill distinct roles in our experiments; the SuperK FIANIUM, having a higher repetition rate, is employed as the quasi-Continuous Wave (CW) white laser source for wavelength sweeping in MIM (Microwave Impedance Microscopy) signal generation, while the SuperK COMPACT, with its lower repetition rate, is utilized as the pulsed white laser source for time-resolved measurement, allowing us to determine the lifetimes of photoresponses.

The SuperK FIANIUM's repetition rate of 78MHz corresponds to a period of about 10ns, making it particularly suitable as a quasi-CW laser source. This period is shorter than the typical lifetimes of TMDs' (Transition Metal Dichalcogenides) photoresponses, which can range from tens of nanoseconds to even microseconds. This allows us to modulate this quasi-CW laser with a mechanical chopper, thereby facilitating the use of lock-in amplifiers for the swift and convenient extraction of demodulated MIM signals. An illustration of the laser system, as assembled in the ECE MRSEC lab, is provided in Figure 3.6.

The SuperK COMPACT, on the other hand, has a 20kHz repetition rate, corresponding to a 50μs period. This longer period ensures that the dynamics of photoresponses, occurring over nanoseconds to microseconds, can be captured after

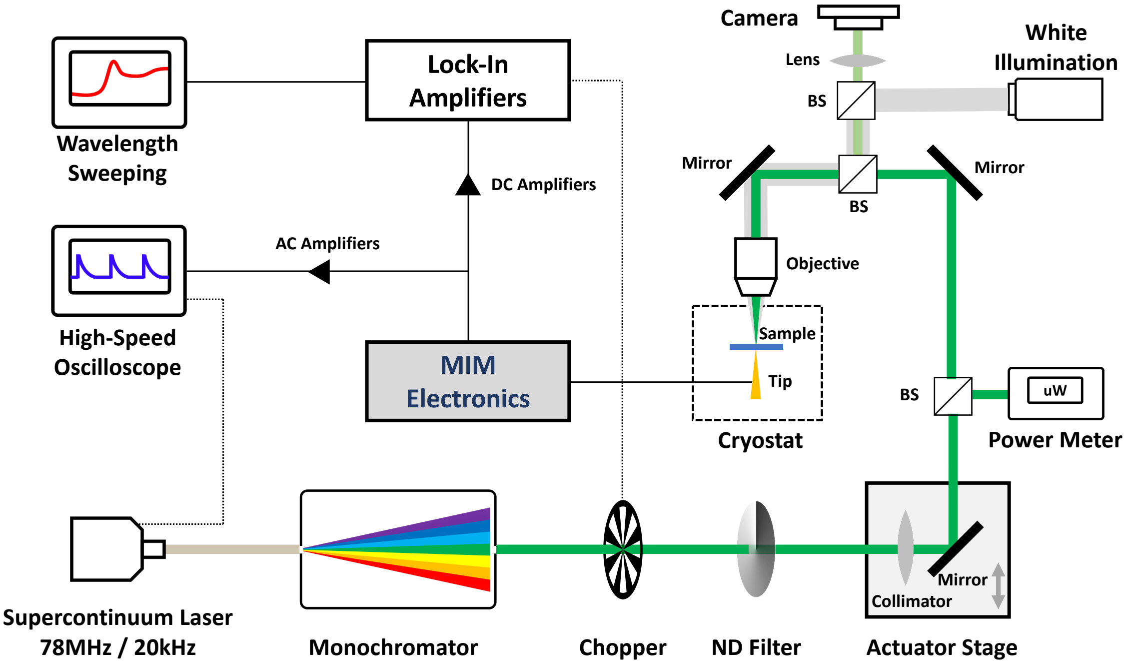

Figure 3.6: Schematic of the spectroscopy iMIM system

one pulse but before the arrival of the next. For this purpose, a high-speed oscilloscope is employed to capture and average the dynamics to accurately ascertain the lifetimes of the photoresponses. It should be noted that this procedure, due to its time-resolution requirements, tends to take significantly longer time than obtaining lock-in readings with the quasi-CW laser.

To facilitate the sweeping of wavelengths, we incorporate the use of a monochromator, specifically model 9055 by Sciencetech Inc, which has a coverage range of 300-1800nm. This device allows us to selectively choose wavelengths from the broad spectrum of white light produced by our SuperK laser sources. An important aspect to note about the monochromator is that, despite its impressively minute mechanical drift (which is typically inconsequential for a defocused laser pattern), this drift becomes noticeable when focusing the laser to a sub-10 micrometer spot on the sample

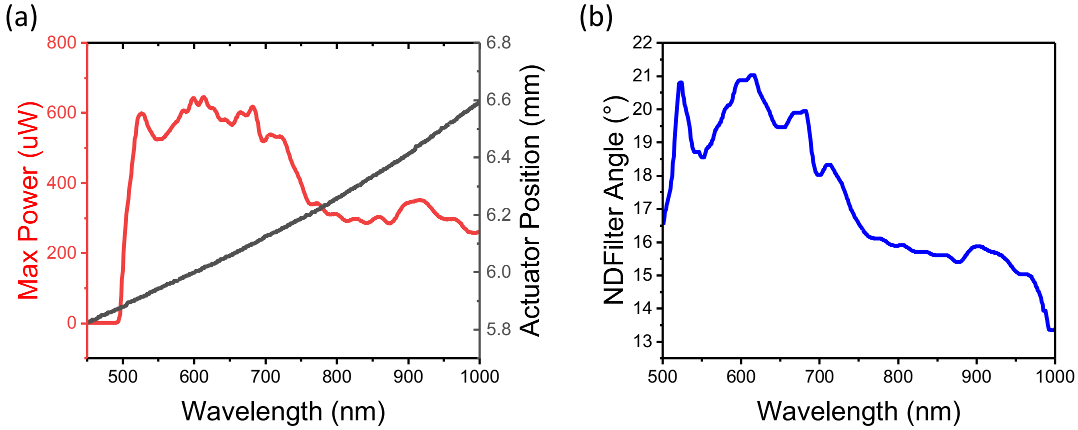

Figure 3.7: (a) Calibration of actuator for monochromator drift compensation, and max power spectrum for SuperK Fianium. (b) Calibration of NDFilter angle for constant laser power (250μW).

- a requirement for achieving high laser intensities. This potential drift needs to be taken into account when maintaining a constant laser intensity during a wavelength sweep.

To address this issue, we have incorporated a motorized translation stage (MT1-Z8 with DC servo motor actuator Z812B by Thorlabs, Inc.) to counterbalance the monochromator's drift. Calibration of this compensatory system can be achieved using a multimode laser fiber, which serves as a laser position alignment paradigm on the end of the translation stage. The fiber will only capture the laser when the translation stage accurately follows the monochromator drift. A depiction of this alignment is provided in Figure 3.7 (a).

The single-wavelength output emanating from the monochromator is then directed through a continuously variable metallic neutral density filter (ND Filter), which is mounted on a motorized rotation mount (K10CR1 by Thorlabs, Inc.). This ND Filter plays a crucial role as a laser intensity adjuster. This function is crucial since the power output of the supercontinuum white laser sources can vary substantially across different wavelengths, as illustrated in Figure 3.7 (a).

To ensure that a constant power is maintained during wavelength sweeps, it is essential to prevent changes in the laser power incident on the sample. Therefore, we need to filter different percentages of the incident power across different wavelengths by fine-tuning the angle of the round continuously variable ND Filter. This process ensures that the power incident on the sample remains consistent irrespective of the wavelength, thereby facilitating reliable and repeatable results. A typical ND Filter calibration for a constant power is shown in Figure 3.7(b).

The process of implementing iMIM spectroscopy involves a series of meticulous steps, each contributing to the overall precision and accuracy of the measurements. This technique, which combines the principles of microwave impedance microscopy with the versatility of optical illumination, allows for a comprehensive analysis of a sample's electrical properties across a range of wavelengths.

The initial stage of the procedure involves the alignment of the tip, laser spot, and sample. This is a crucial step as it ensures that the laser light is accurately focused on the sample and that the tip is in the correct position for optimal signal detection. The alignment process is similar to that described in Section 3.1, and it requires careful manipulation of the experimental setup to achieve the desired configuration.

Once the alignment is completed, the next step is to approach the sample with the tip. This is done using the same method as described in the aforementioned section. Depending on the laser source being used, the output from the MIM electronics is connected to either DC amplifiers and Lock-In amplifiers (when using the SuperK FIANIUM laser source) or AC amplifiers and the oscilloscope (when using the SuperK COMPACT laser source).

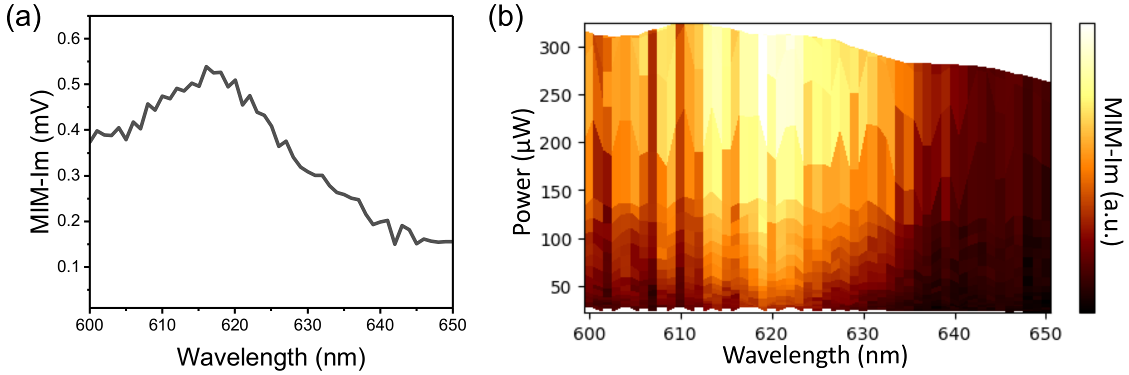

Figure 3.8: iMIM spectroscopy of a WS_2 monolayer. (a) iMIM spectrum with a constant laser power (250μW) (b) Heatmap of iMIM with varying power and wavelength

In the case of the SuperK FIANIUM laser source, we designed and created the dedicated SpectraDynamics software equipment control and initialization, as well as for the collection and analysis of data. The software allows for the configuration of various parameters such as the step size (typically set to 1nm) and the number of reading averages (typically set to 100). This process enables the acquisition of demodulated iMIM signals as the wavelength is swept across the desired range.

When using the SuperK COMPACT laser source, the oscilloscope is set to the maximum averaging number and a suitable reading average is set in the software. Due to the lower repetition rate of the SuperK COMPACT, this process typically takes longer than when using the SuperK FIANIUM. However, the lower repetition rate is necessary to ensure that the photoresponse has fully decayed before the arrival of the next pulse.

The SpectraDynamics software offers several modes for controlling the wavelength sweep. One option is to sweep the ND Filter for each individual wavelength, which allows for the acquisition of a heatmap of demodulated iMIM signals as a function of both power and wavelength, as shown in Figure 3.8(b). However, this process can be time-consuming, especially when a high signal-to-noise ratio is required.

Alternatively, a constant power mode can be used, which involves dynamically adjusting the power for different wavelengths using the actuator and ND Filter. This process requires a calibration scanning step to determine the appropriate angle of the ND Filter for each wavelength to achieve the target power, as shown in Figure 3.7(b). Once calibrated, the software can control the monochromator, actuator, and ND Filter in parallel to save time and get a spectrum with averaging at a fixed power, as shown in Figure 3.8(a).

The entire setup, including the piezo stack, tip, and sample, is enclosed in the ST500 cryostat, which allows for wavelength sweeping at low temperatures. For measurements above 90 Kelvin, liquid nitrogen is used as the cooling liquid, providing a sufficiently low temperature environment without the need for more complex cooling systems. For instances where even lower temperatures may be required for specific experimental conditions or for studying certain material properties, we can resort to using liquid helium as the cryogen, which can effectively cool down the system to temperatures as low as 30 Kelvin or even lower.

In essence, iMIM spectroscopy is a powerful and versatile tool that opens up new possibilities for research in a variety of fields, from condensed matter physics to materials science. By offering a comprehensive platform for investigating material properties across a wide range of wavelengths and temperatures, this technique provides researchers with a wealth of information that can be used to gain a deeper understanding of the materials under study. The potential applications of iMIM spectroscopy are vast, and it is anticipated that this technique will continue to play a pivotal role in advancing our knowledge of material properties in the years to come.

Projects leveraging the capabilities of iMIM spectroscopy will be explored in Chapter 5.

Chapter 4: Spatiotemporal Dynamics of Photocarriers in Perovskites

Perovskites and two-dimensional (2D) semiconductors, especially transition metal dichalcogenides (TMDs), are at the forefront of materials science and nanotechnology research. These materials possess unique properties that position them as promising contenders for diverse applications, including photovoltaics, optoelectronics, and quantum computing. However, to fully harness their potential, a comprehensive understanding of their intrinsic photoelectric properties at the nanoscale is essential.

This is where innovative tools like light-illuminated microwave impedance microscopy (iMIM) become invaluable. iMIM offers a non-invasive approach to explore these properties, providing critical insights into the behavior of these materials under varying conditions. Unlike scanning photocurrent microscopy (SPCM), which requires additional physical metal contact and potentially introduces extrinsic properties, iMIM facilitates non-intrusive and direct intrinsic measurements. This makes iMIM an indispensable tool for researchers in the field, enabling them to study these fascinating materials in a more precise and less disruptive manner.

In this and the subsequent chapters, I will delve into two papers that employ iMIM techniques to investigate the optoelectronic properties of perovskites and 2D TMD semiconductors. Both papers are the ones in which I am the first author, and my contributions spanned the design of the research, execution of the experiments, analysis of the data, and authoring of the manuscripts. The first paper in this chapter is as below. The second paper to be discussed in the next chapter is the manuscript to be published.

Paper adapted in this chapter:

Ma, X., Zhang, F., Chu, Z., Hao, J., Chen, X., Quan, J., Huang, Z., Wang, X., Li, X., Yan, Y. and Zhu, K. Superior photo-carrier diffusion dynamics in organic-inorganic hybrid perovskites revealed by spatiotemporal conductivity imaging. *Nature Communications* **12**, 5009 (2021). https://doi.org/10.1038/s41467-021-25311-1

The outstanding performance of organic-inorganic metal trihalide solar cells benefits from the exceptional photo-physical properties of both electrons and holes in the material. Here, we directly probe the free-carrier dynamics in Cs-doped $FAPbI_3$ thin films by spatiotemporal photoconductivity imaging. Using charge transport layers to selectively quench one type of carriers, we show that the two relaxation times on the order of 1 μs and 10 μs correspond to the lifetimes of electrons and holes in $FAPbI_3$, respectively. Strikingly, the diffusion mapping indicates that the difference in electron/hole lifetimes is largely compensated by their disparate mobility. Consequently, the long diffusion lengths (3-5 μm) of both carriers are comparable to each other, a feature closely related to the unique charge trapping and detrapping processes in hybrid trihalide perovskites. Our results unveil the origin of superior diffusion dynamics in this material, crucially important for solar-cell applications.

4.1 Materials

All solvents were purchased from Sigma-Aldrich and used as-received without any other refinement. Formamidinium iodine (FAI) was purchased from Greatcell Solar. Lead iodide (PbI2) was from TCI Corporation. Spiro-OMeTAD was received from Merck Corporation. Cesium iodine (CsI) and PTAA were purchased from Sigma-Aldrich. Patterned fluorine-doped tin-oxide-coated (FTO) glass (<15 Ω/square) and indium tin-oxide-coated (ITO) glass were obtained from Advanced Election Technology Co., Ltd.

4.2 Sample preparation

The perovskite films in this work were deposited on top of cover glasses or ITO glass. The substrate glasses were cleaned extensively by deionized water, acetone, and isopropanol. For the HTL deposition, the PTAA (Sigma-Aldrich) was dissolved in toluene with a concentration of 5 mg mL^{-1} and spin-coated on the substrates at 5000 rpm for 30 s. The spun PTAA films were annealed at 100 °C for 10 min. For the ETL deposition, a compact titanium dioxide (TiO_2) layer of about 40 nm was deposited by spray pyrolysis of 7 mL 2-propanol solution containing 0.6 mL titanium diisopropoxide bis(acetylacetonate) solution (75% in 2-propanol, Sigma-Aldrich) and 0.4 mL acetylacetone at 450 ˚C in air. The FA0.95Cs0.05PbI3 precursor solution was prepared by dissolving 0.4 M Pb^{2+} in dimethyl sulfoxide (DMSO) and dimethylformamide (v/v = 3/7) mixed solvent. Perovskite films were deposited using a three-step spin-coating procedure with the first step of 100 rpm for 3 s, the second step of 3500 rpm for 10 s, and the last step of 5000 rpm for 30 s. Toluene (1 mL) was applied on the spinning substrates at 20 s of the third step. After spin coating, the substrates were annealed at 170 ˚C for 27 min. The encapsulated perovskite films were capped with PMMA (Mw about 120,000) film by spin-coating 15 mg ml^{-1} PMMA in chlorobenzene solution at 4000 rpm for 35 s.

4.3 Background

Organic-inorganic lead trihalide perovskite solar cells (PSCs) have been in the limelight of photovoltaic research [22–24], as exemplified by the outstanding certified power conversion efficiency (PCE) that exceeds 25% to date [25]. Even in the polycrystalline form, the PSC thin films exhibit many remarkable photo-physical properties, such as high absorption coefficient [26], long carrier lifetimes [27], and low impurity scattering rate [28, 29]. For photovoltaic applications, a particularly attractive feature of hybrid perovskites is that both electrons and holes are active in the photoconduction process [27–31]. From the theoretical point of view, the two types of carriers are expected to exhibit comparable effective mass, intrinsic mobility, recombination lifetime, and diffusion length [32–34]. In real materials, however, the balance between electrons and holes is usually broken by thin-film deposition conditions, defect structures, ionic disorders, and other sample-dependent parameters [35–38], which may affect the photo-carrier extraction in functional devices. A thorough understanding of the dynamics of individual charge carriers is thus imperative for continuous improvements of PSC performance towards commercial applications.

The spatiotemporal dynamics of electrons and holes in optoelectronic materials are widely studied by optical measurements such as time-resolved photoluminescence (TRPL) and transient absorption spectroscopy (TAS) [29–31, 39, 40]. The diffusion length can then be deduced by fitting the results to a diffusion model [29–31]. It should be noted that TRPL and TAS probe optical excited states and are often dominated by transitions with large oscillator strength. In contrast, the transport of photoexcited carriers is electrical and quasi-static in nature. In order to directly evaluate photoconduction, it is common to measure the photocurrent across electrical contacts, such as scanning photocurrent microscopy (SPCM) [37, 41, 42]. The spatial resolution of SPCM is diffraction-limited and the temporal response is dominated by the carrier transit time and extrinsic metal-semiconductor Schottky effect. In recent years, noncontact methods such as time-resolved microwave conductivity (TRMC) [27, 28, 37, 43–46] and time-resolved THz spectroscopy (TRTS) [38, 47] are developed to probe the photocarrier dynamics. These far-field techniques, however, do not offer spatially resolved information such as diffusion patterns.

In this article, we directly probe free-carrier diffusion dynamics in Cs-doped formamidinium (FA) lead trihalide ($FAPbI_3$) thin films by laser-illuminated microwave impedance microscopy (iMIM), a unique optical-pump-electrical-probe technique with 20-nm spatial resolution and 10-ns temporal resolution for the electrical detection [48]. The steady-state iMIM experiment addresses the most important photo-physical process in solar cells, i.e., the transport of photo-generated mobile carriers under the continuous illumination of ∼1 Sun. The time-resolved iMIM (tr-iMIM) experiment detects the free-carrier lifetime that is also highly relevant for photoconduction. By depositing a hole or electron transport layer (HTL/ ETL) underneath $FACsPbI_3$, we show that the two decay constants in tr-iMIM measurements are associated with the lifetimes of electrons and holes. The spatiotemporal imaging allows us to determine the diffusion coefficients, steady-state carrier density, and mobility of individual carriers. Interestingly, while the lifetime and mobility of electrons and holes differ substantially, their products and thus the diffusion lengths are comparable to each other, which is likely due to the unique defect structures and charge trapping events in PSC thin films. Our results highlight the origin of nearly balanced diffusion dynamics of electrons and holes in hybrid trihalide perovskites, which is highly desirable for photovoltaic applications.

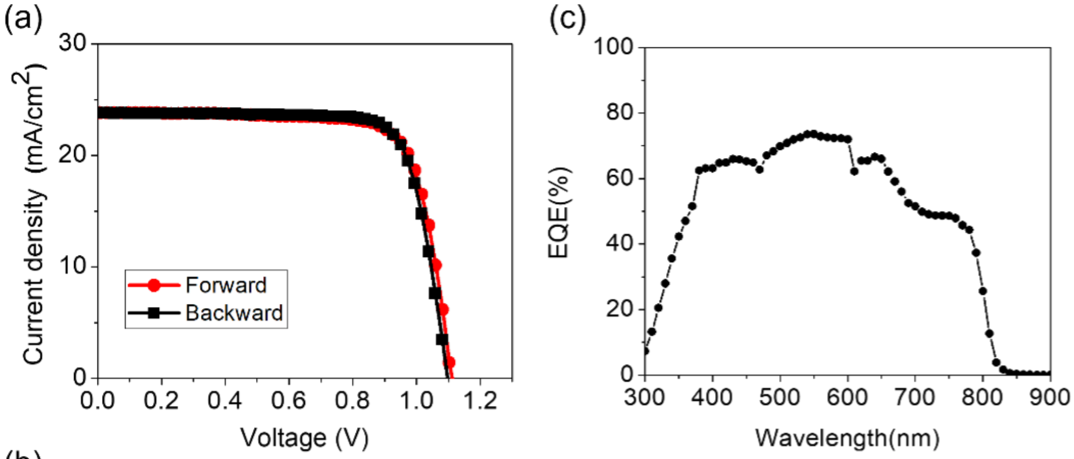

(b)

Direction	J_{SC} (mA·cm^{-2})	V_{OC}(V)	*FF*	*PCE*(%)
Forward	23.81	1.10	0.77	20.2
Backward	23.79	1.10	0.78	20.4

Figure 4.1: Standard AM1.5 solar cell device performance. (a) I-V characteristics of the solar cell device made from the 550-nm-thick $FA_{0.95}Cs_{0.05}PbI_3$ thin films. (b) Table of the device parameters, listing the short-circuit current density Jsc, open-circuit voltage Voc, fill factor (FF), and PCE of both films. (c) External quantum efficiency (EQE) spectra of the 250-nm-thick $FA_{0.95}Cs_{0.05}PbI_3$ thin film. Panels a-c and captions are from Ref. [4] with permission.

4.4 iMIM Results

The PSC thin film in this study, hereafter labeled as Sample A, is 5% Cs-doped FA lead triiodide deposited on cover glasses (see Methods). Compared with methylammonium (MA) based perovskites, $FAPbI_3$ exhibits superior stability at elevated temperatures and an ideal band gap for sunlight absorption [49]. The Cs-doping further stabilizes the room-temperature photo-active α-phase by reducing the Goldschmidt tolerance factor [50–53]. Perovskite films were deposited using the typical anti-solventassisted spin-coating procedure. The samples were then capped by spin-coating 15 mg ml^{-1} PMMA (Mw $\sim$ 120,000) film in chlorobenzene solution. For iMIM measurements, we chose a film thickness of d = 250 nm that is greater than the absorption length, such that light is fully absorbed, but much less than the carrier diffusion length, such that the photoconductivity is uniformly distributed in the vertical direction within the relevant time scale in our experiment. External quantum efficiency (EQE) spectra were also measured (Fig. 4.1), showing good photoresponse across the solar spectrum. PSC devices made from the same material but with thicker film (550 nm) demonstrated a PCE above 20% under the standard air mass (AM) 1.5 illumination (Fig. 4.1).

Solar cell performance measurements were taken under a simulated AM 1.5G illumination (100 mW/cm^2, Oriel Sol3A Class AAA Solar Simulator). The photocurrent density–voltage (J–V) characteristics were measured using a Keithley 2400 source meter. The J–V curves of all devices were measured by masking the active area with a metal mask of area 0.12 cm^2. Both backward-scan and forward-scan curves were measured with a bias step of 10 mV and delay time of 0.05 s. Typical J–V curves are shown in Fig. 4.1a and the results are summarized in Fig. 4.1b, for 550-nm-thick perovskite based solar cells. Fig. 4.1c shows the external quantum efficiency (EQE) spectra of our 250-nm-thick $FA_{0.95}Cs_{0.05}PbI_3$ thin films measured by a solar cell quantum-efficiency measurement system (QEX10, PV Measurements).

The spatiotemporal iMIM setup with a focused laser beam illuminating from below the sample stage is illustrated in Fig. 4.2a. In the tip-scan mode, the laser is focused by one set of piezo-stage and the second piezo-scanner carries the tip to scan over the sample [48]. In the sample-scan mode, the first set of piezo-stage aligns the center of the laser spot to the tip, whereas the sample is set in motion by the piezo-scanner [54, 55]. In both configurations, one can fix the relative position between tip and sample and perform time-resolved (tr-iMIM) measurements [48].

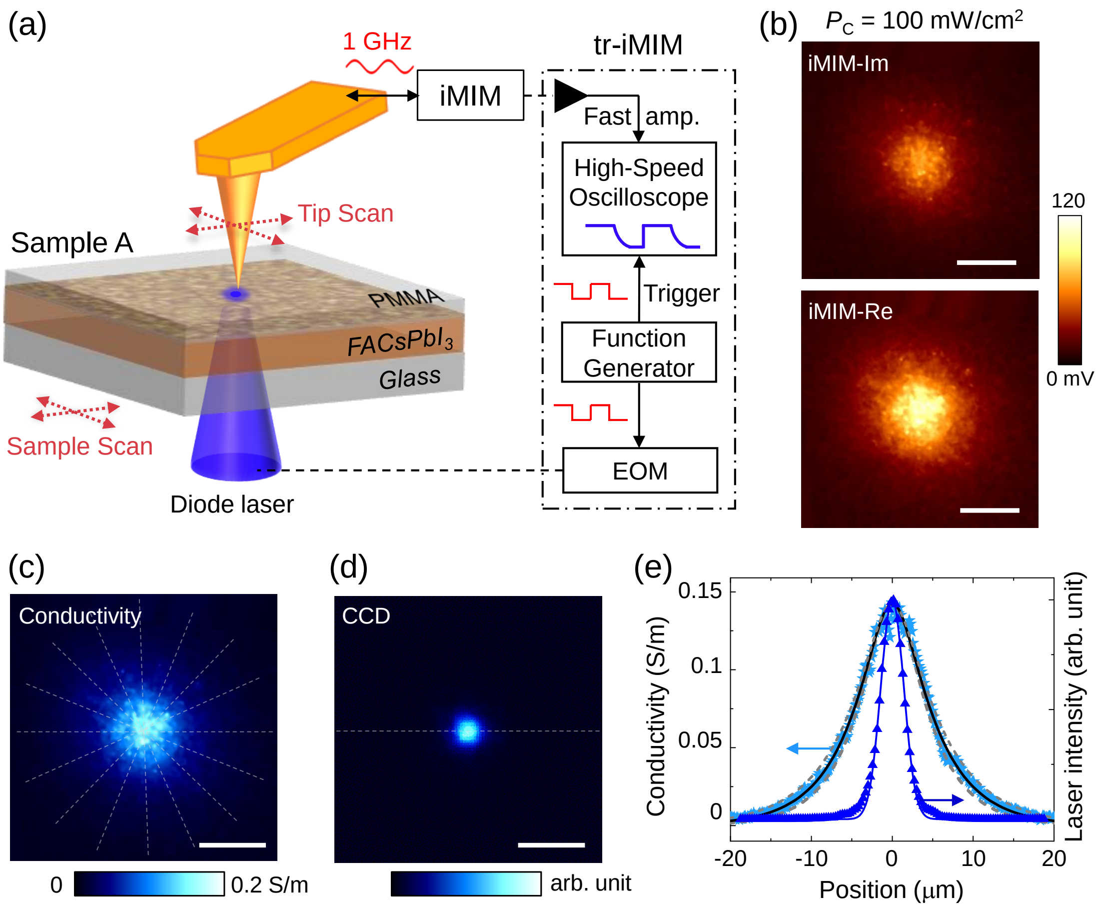

Figure 4.2: Photoconductivity mapping on $FACsPbI_3$ and diffusion analysis. a Schematic of the iMIM setup with either the tip-scan or sample-scan mode. The tr-iMIM configuration is shown inside the dash-dotted box. The $FACsPbI_3$ thin film deposited on a glass substrate and encapsulated by a PMMA layer (Sample A) is also illustrated. b Tip-scan iMIM images when the sample is illuminated by a 446-nm diode laser at $P_C = 100$ mW/cm^2. c Photoconductivity map based on the iMIM data and FEA simulation. The dashed lines are various linecuts for the calculation of average signals. d Image of the laser spot taken by a CCD camera. e Line profiles of averaged photoconductivity and laser intensity, from which the diffusion length can be extracted. The solid black and dashed gray lines represent the best curve fitting and upper/lower bounds, respectively. All scale bars are 10 μm. Panels a-e and captions are from Ref. [4] with permission.

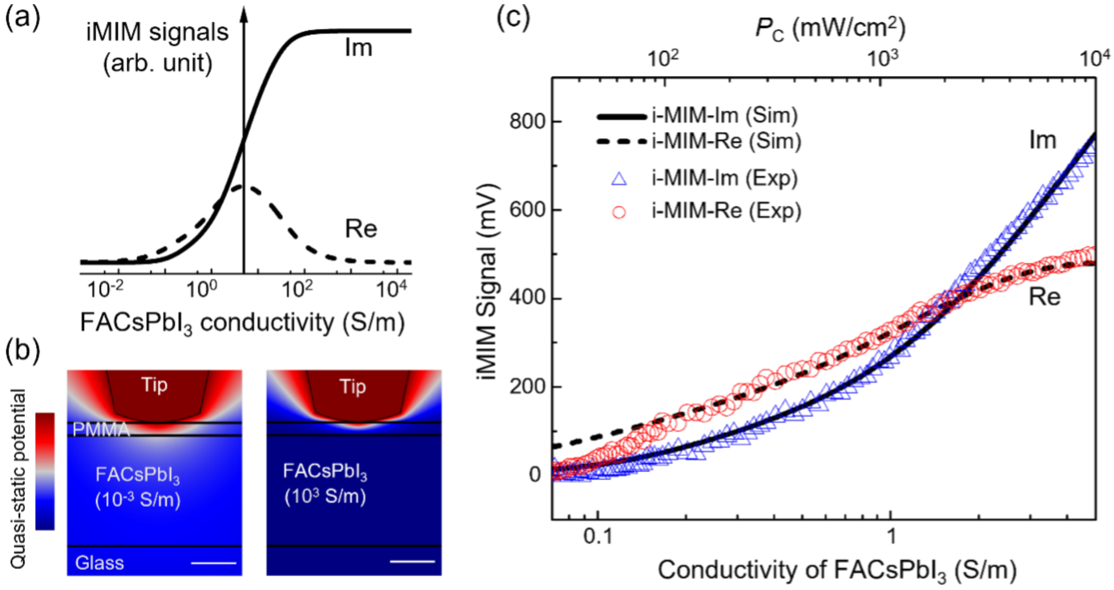

Figure 4.3: Comparison between experimental data and simulation results. (a) Simulated iMIM response as a function of the conductivity of the perovskite layer. (b) Distribution of quasi-static potential near the tip apex at $\sigma = 10^{-3}$ S/m (left) and 10^3 S/m (right). (c) Measured (open circles and triangles) iMIM signals as a function of laser power and simulated (solid and dashed lines) results as a function of the FACsPbI$_3$ conductivity. Note that the photoconductivity does not scale with the illumination intensity. Panels a-c and captions are from Ref. [4] with permission.

Here the laser output is modulated by an electro-optic modulator (EOM), which is driven by a 7-kHz square wave from a function generator such that steady-state photoconductivity is reached in the laser-ON state and zero photoconductivity in the laser-OFF state. The same waveform also triggers a high-speed oscilloscope for iMIM measurement. The temporal resolution of our setup is ~10 ns (see Methods). The microwave electronics detect the tip-sample impedance, from which the local conductivity can be deduced [3]. The optical excitation in our setup is diffraction-limited, whereas the electrical imaging has a spatial resolution of 20–50 nm compared to the tip diameter. Quantification of the iMIM signals by finite-element analysis (FEA) [56] is detailed in Fig. 4.3. As the conductivity σ of $\mathrm{FACsPbI_3}$ increases, the microwave electrical fields are gradually screened by the free carriers. Consequently, the imaginary part of the signal, iMIM-Im (proportional to tip-sample capacitance), increases monotonically with respect to σ, whereas the real-part signal iMIM-Re (proportional to tip-sample conductance) peaks at $\sigma \sim 10$ S/m. As depicted in the insets of Fig. 4.3b, the spread of the quasistatic potential indicates that the spatial resolution of iMIM is comparable to the tip diameter. The conversion from iMIM images to conductivity images is achieved by directly comparing the experimental data and simulated results. To this end, we performed a point measurement on Sample A and measured the iMIM signals as a function of the laser intensity. As plotted in Fig. 4.3c, the response curve computed by FEA (iMIM signals versus conductivity) and the experimental data (iMIM signals versus laser power) are in excellent agreement over a wide range of parameter space1. We can therefore replot the raw iMIM images to photoconductivity maps with high conversion fidelity.

Figure 4.2b shows the iMIM images when Sample A was illuminated by a 446-nm ($h\nu = 2.78$ eV) diode laser with the intensity at the center of the laser spot

$P_C = 100$ mW/cm^2, i.e., on the order of 1 Sun. The granular features are due to topographic crosstalk with the polycrystalline sample surface [54]. It is nevertheless evident that the photoresponse is continuous across many grain boundaries (GBs). Based on the iMIM response (Supplementary Fig. 2), we can replot the data to a conductivity map (Fig. 1c) with high conversion fidelity. For comparison, the optical image of the laser spot acquired from a charge-coupled device (CCD) camera shows a much smaller spatial spread in Fig. 1d. To improve the signal-to-noise ratio and minimize the topographic artifact, we averaged eight line profiles shown in Fig. 1c. The resultant curve, plotted in Fig. 1e, is clearly broader than the Gaussian beam profile (e^{-r^2/w^2} , $w \sim 2\mu$m). Assuming that the carrier mobility mu is independent of charge density n within the range of our experiment, the measured photoconductivity profile σ(r) is proportional to the steady-state density profile n(r) as

$$\sigma(r) = n(r)q\mu \tag{4.1}$$

where q is the elemental charge. Here $n(r)$ can be described by the diffusion equation [48, 57, 58].

$$n(r) - L^2\nabla^2 n(r) = \frac{\eta}{d}\frac{P_c\tau}{h\nu}e^{-r^2/w^2} \tag{4.2}$$

where $L = \sqrt{D\tau}$ is the diffusion length, D the diffusion coefficient, τ the lifetime, and $eta \sim 1$ he incident photon-to-current conversion efficiency (IPCE). The analytical solution to Eq. (4.2) is

$$n(r) \propto \int_{-\infty}^{\infty} K_0(r'/L)e^{-(r-r')^2/w^2}dr' \tag{4.3}$$

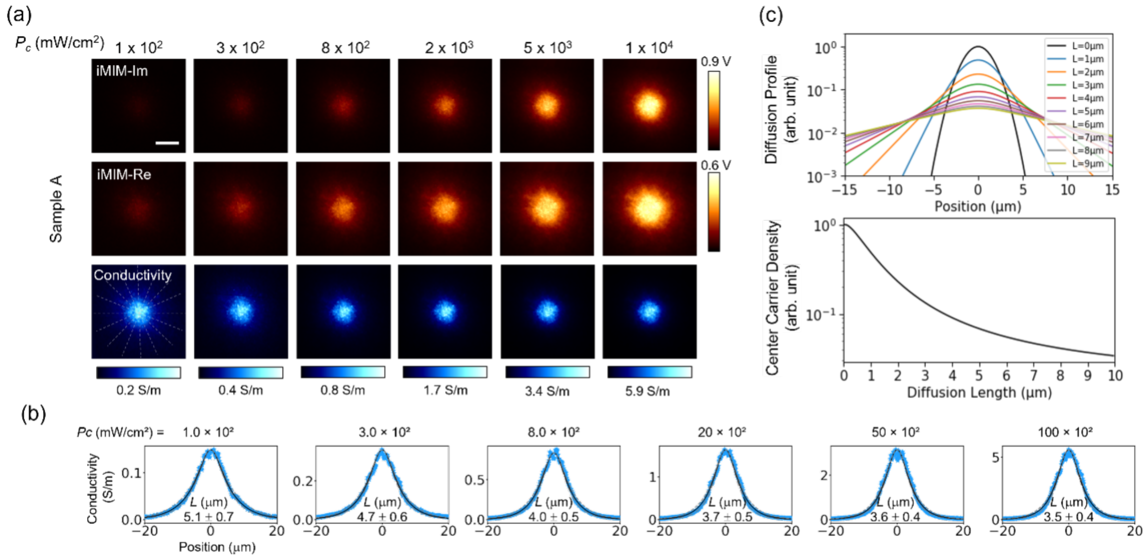

Figure 4.4: Power-dependent diffusion mapping for Sample A. (a) Power-dependent iMIM-Im/Re and photoconductivity images of Sample A. (b) Line profiles of averaged photoconductivity and laser intensity and curve fittings, from which the diffusion lengths can be extracted. (c) (Upper panel) Spatial distribution of charge carriers with various diffusion lengths. (Lower panel) Carrier density at the center of the illumination spot as a function of diffusion length. Panels a-c and captions are from Ref. [4] with permission.

where K_0 is the modified Bessel function of the second kind. By fitting the iMIM data to Eq. (4.3), we obtain a diffusion length $L = 5.1 \pm 0.6\mu$m, consistent with values reported in the literature for thin-film PSCs [30, 31, 37, 59]. As the laser power increases, L decreases to ∼4 μm at $P_C \sim 10^3$ mW/cm^2 and saturates at 3.5 μm for $P_C \sim 10^4$ mW/cm^2 (Fig. 4.4).

The power-dependent iMIM-Im/Re images of Sample A are shown in Fig. 4.4a. As depicted in Fig. 4.4b, the curve fitting to Eq. (4.3) in the main text allows us to obtain the diffusion lengths at different laser power. Using Eqs. (4.2) and (4.3) in the main text, we can quantitatively analyze the diffusion pattern. Fig. 4.4c shows the spatial distribution of charge carriers with various diffusion lengths under an excitation profile e^{-r^2/w^2} with $w \sim 2\mu$m. For instance, assuming $n_{c_0} = \eta(P_c\tau/h\mu)$ is the density at the center of laser spot for $L = 0\mu$m, the numerical solution indicates that $n_c \sim 0.07n_{c_0}$ for $L = 5\mu$m. The analysis is important for the calculation of carrier density and mobility, which are tabulated in Fig. 4.11d.

Figure 4.5a shows a typical tr-iMIM decay curve (averaged over 242,880 cycles) on Sample A illuminated by the 446-nm laser at PC = 100 mW/cm^2 before t = 0. As the iMIM-Im signal scales with photoconductivity in our measurement range (Fig. 4.6), we will just present the raw data in the following analysis. From Eq. (4.1), the decay of tr-iMIM-Im signal provides a direct measure of the lifetime of mobile carriers in the conduction or valence band. The relaxation fits nicely to a biexponential function $y = A_1e^{-t/\tau_1} + A_2e^{-t/\tau_2}$, with $\tau_1 \sim 0.7$ μs and $\tau_2 \sim 10$ μs.

We also performed tr-iMIM experiments with two additional diode lasers with wavelengths of 517 nm (green) and 638 nm (red). As shown in Fig. 4.7, the two relaxation time constants in Sample A were observed in all three measurements. It is possible that the thermalization to the band edge through phonon emitting is

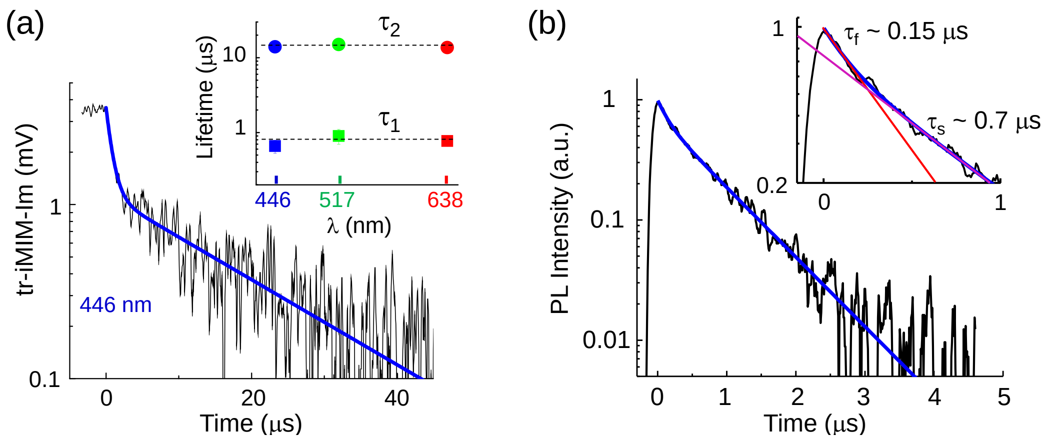

Figure 4.5: Time-resolved iMIM and carrier lifetime. (a) Typical tr-iMIM relaxation curve of Sample A. The sample was illuminated by the 446-nm laser at P_C = 100 mW/cm^2 before t = 0 μs. The inset shows the two lifetimes under excitation lasers with wavelengths of 446, 517, and 638 nm. (b) TRPL data of Sample A. The blue curve is a biexponential fit to the TRPL data. The inset is a close-up view, showing the two decay time constants from the fitting. Panels a-b and captions are from Ref. [4] with permission.

very effective at low laser intensities ($\sim$ 1 Sun), after which the trapping/detrapping processes take place. As a result, the carrier temperature is essentially independent of the excitation wavelength. We therefore conclude that the two lifetimes are intrinsic for the FACsPbI$_3$ thin films. As shown in the inset of Fig. 4.5a, we observed the same τ_1 and τ_2 when using 517-nm and 638-nm lasers (Fig. 4.7), suggesting that the time constants are intrinsic to the sample and independent on the laser wavelength. In contrast, the TRPL data on Sample A (Fig. 4.5b) exhibit two different times $\tau_f \sim$ 150 ns and $\tau_s \sim 0.7$ μs, which will be discussed in the next section. By parking the tip at various locations of the film and measuring the decay curves, we also show that the tr-iMIM response is spatially uniform on the sample surface within statistical errors (Figs. 4.8 and 4.9).

For the point experiment shown in Fig. 4.5, we used an ultra-sharp tip from

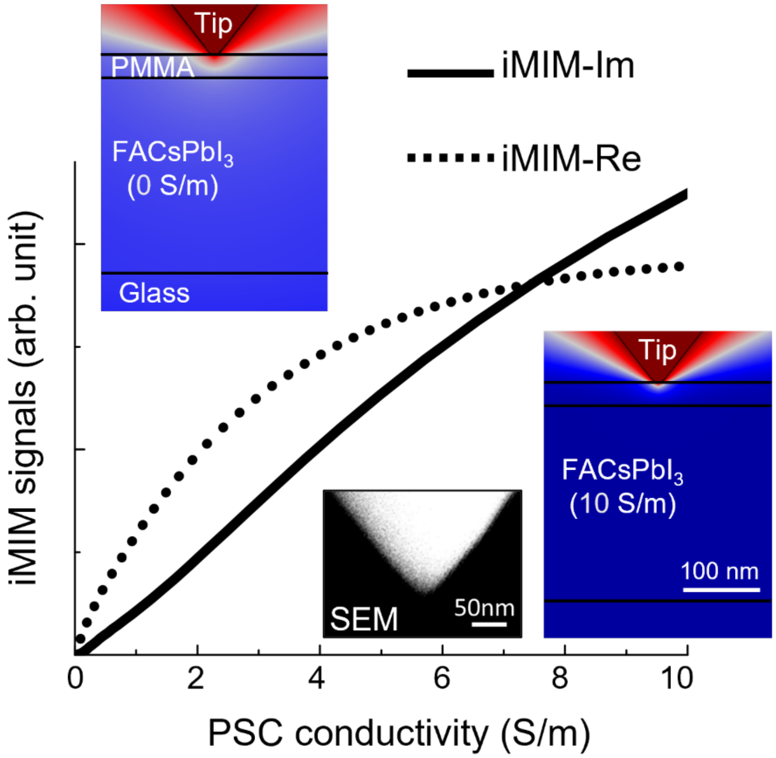

Figure 4.6: Simulated iMIM response for the ultra-sharp tip as a function of the conductivity. Distributions of quasi-static potential are shown at $\sigma = 0$ S/m (left) and 10 S/m (right). Panel and caption are from Ref. [4] with permission.

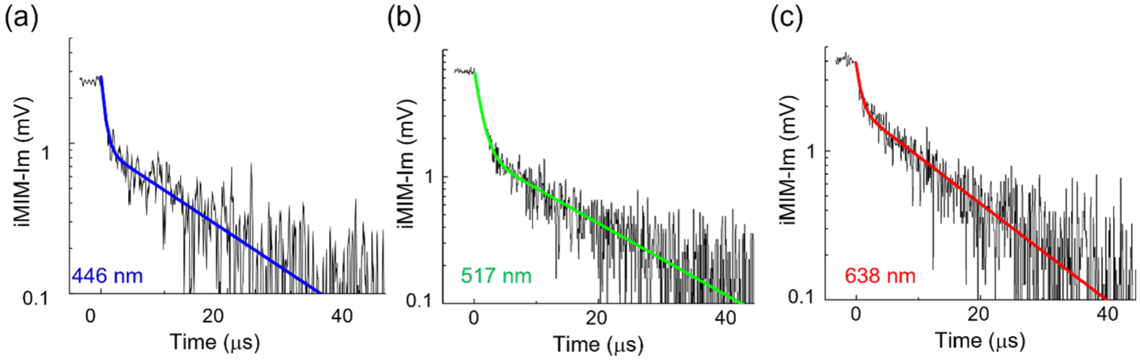

Figure 4.7: Wavelength-dependent tr-iMIM-Im signals with laser intensity ∼100 mW/cm^2. Panels a-b and captions are from Ref. [4] with permission.

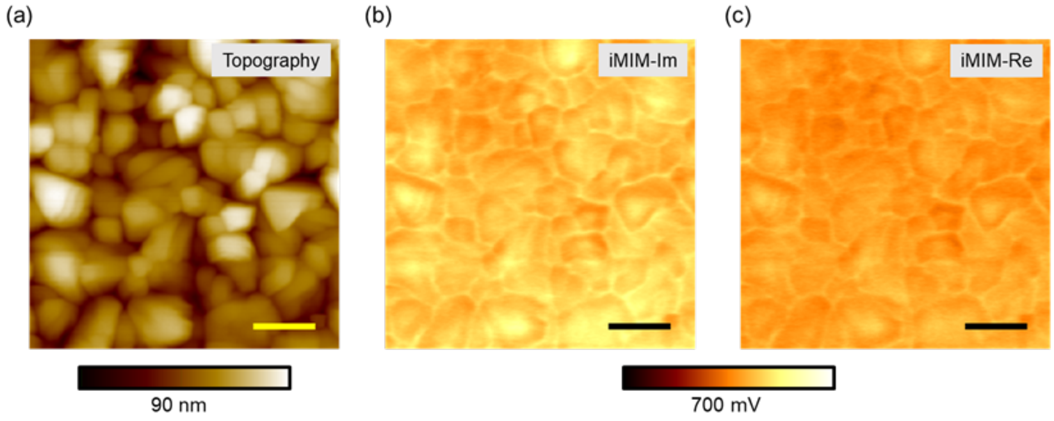

Figure 4.8: Raw AFM and iMIM-Im/Re images of sample A. (a) AFM, (b) iMIM-Im, (c) iMIM-Re images. All scale bars are 4 μm. Panels a-c and captions are from Ref. [4] with permission.

Rocky Mountain Nanotechnology LLC, model 12PtIr400A-10 with a nominal radius of 10 nm at the apex, for accurate positioning on grains and grain boundaries. For the FEA modeling, we have used the half-angle of 38° and a diameter of 20 nm at the apex that are consistent with the SEM image. As shown in Fig. 4.6, the simulated iMIM-Im signals roughly scales with the conductivity of $FACsPbI_3$ up to $\sigma \sim 10$ S/m, which is within the photoconductivity range in our experiment. As a result, we directly analyze the tr-iMIM-Im signals rather than converting them to photoconductivity in the time-resolved response.

In order to shed some light on the tr-iMIM data, we studied the carrier dynamics in perovskite thin films with electron or hole transport layers [27, 28, 30, 31, 43, 44]. For the HTL sample, hereafter referred to as Sample B, a 20-nm PTAA (poly-triaryl amine) was spincoated on the substrate before the same 250-nm $FACsPbI_3$/30-nm PMMA film was deposited. The PTAA layer rapidly extracts photo-generated holes from $FACsPbI_3$ within a sub-10-ns time scale [43, 44, 60]. Similarly, a 40-nm ETL TiO_2 layer for the extraction of electrons was coated on the substrate before the

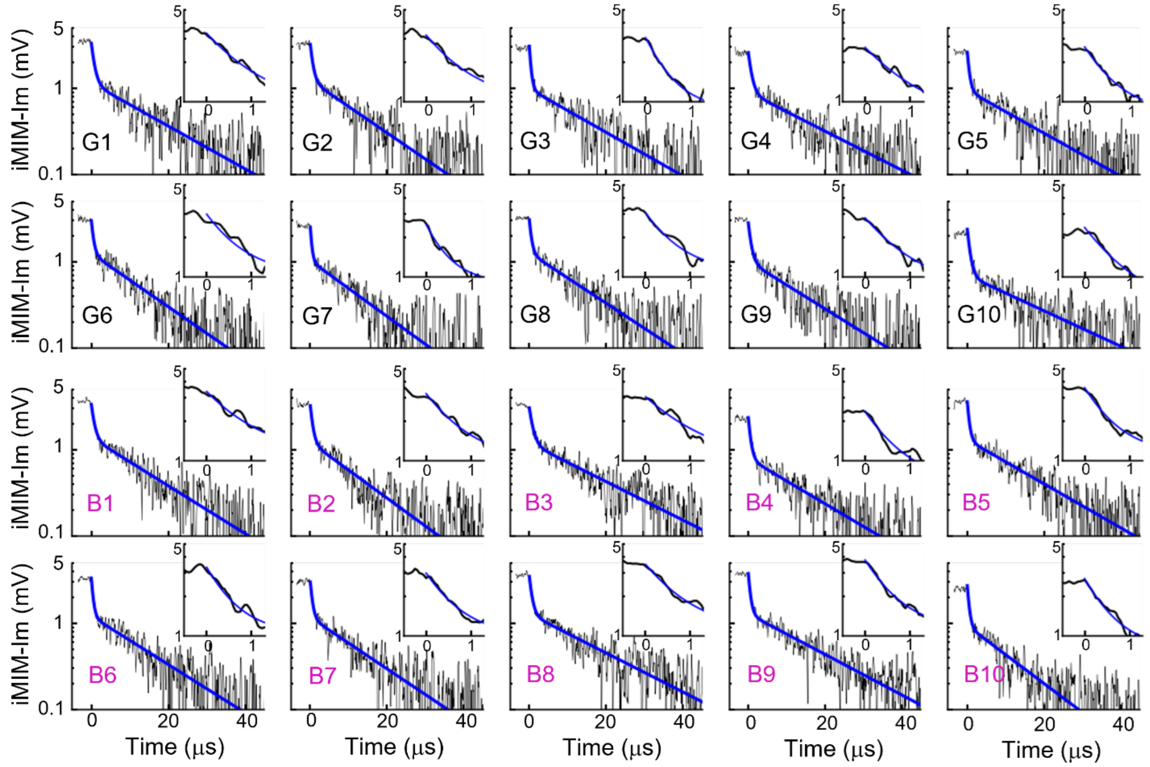

Figure 4.9: Complete set of tr-iMIM-Im data for 20 points. G1-G10 are points on grains, while B1-B10 are points on grain boundaries. Panels and captions are from Ref. [4] with permission.

$FACsPbI_3$/ PMMA deposition for Sample C. Control experiments have been conducted to ensure that the PL is quenched in both Samples B and C due to the extraction of holes and electrons, respectively (Fig. 4.10). the PL signal is quenched by 94% in the PTAA/$FACsPbI_3$ Sample B and 80% in the TiO_2/$FACsPbI_3$ Sample C. It should be noted that, for good signal-to-noise ratio, the excitation power (9.6×10^3mW/cm^2, on the order of 100 Sun) is kept high in the PL experiments. The incomplete PL quenching in Samples B and C is consistent with the high-power tr-iMIM data in Fig. 4.16. Note that the charge dynamics in the transport layers ($\sim$300 nm below the surface) would not affect the iMIM results due to the shallow probing depth of 50–100 nm. The tr-iMIM data in Samples B and C under the 446-nm laser illumination with PC = 100 mW/cm^2 are shown in Fig. 4.11a. It is evident that only the fast process with $\tau_1 \sim 0.7$ μs survives in Sample B and the slow process with $\tau_2 \sim$ 10 μs in Sample C. The observation strongly suggests that the two time constants in Sample A are associated with the lifetime of electrons and holes in $FACsPbI_3$.

The HTL/ETL samples also allow us to separately address the diffusion dynamics of electrons and holes. Figure 3b, c show the tipscan photoconductivity maps of Samples B and C under $P_C = 100$ mW/cm^2, from which $L_e \sim 5.2$ μm and $L_h \sim$ 2.7 μm can be extracted, respectively. As tabulated in Fig. 4.11d, we can derive the diffusion coefficient from the diffusion equation $L = \sqrt{D\tau}$ and carrier mobility ($\mu_{e,diff}$ = 15 cm^2/V·s and ($\mu_{h,diff} = 0.3$ cm^2/V·s) from the Einstein relation $\mu = (q/k_BT) * D$. A different method to analyze the transport properties is through the photoconductivity (Eq. 4.1) and density profile (Eq. 2). The calculated mobility values are $\mu_{e,pc} = 24$ cm^2/V·s and $\mu_{h,pc} = 0.3$ cm^2/V·s. The small difference between the two methods is within the error bars of the measurements. We note that in $MAPbI_3$ and $FAPbI_3$ thin films, mobility values measured by different techniques vary in a

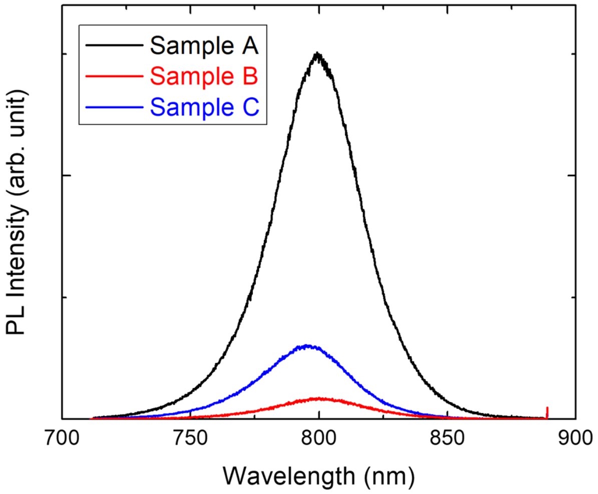

Figure 4.10: PL data on Samples A, B, and C at an excitation laser power of 9.6×10^3mW/cm^2. Panel and caption are from Ref. [4] with permission.

considerable range from 0.2 to 30 cm^2/V·s [27–31, 35, 38, 44–46, 49, 61, 62]. As tabulated in Fig. 4.12, either $\mu_e > \mu_h$ or $\mu_e < \mu_h$ has been reported in the literature. In our experiment, mobility values are directly calculated from the measured L and τ under an illumination intensity lim 1 Sun, with no other assumptions or modeling involved. The pronounced difference between μ_e and μ_h is thus genuine. Figure 3d also indicates that the equilibrium carrier density in our experiment is on the order of $10^{15} - 10^{16}$cm^{-3}. Within this range, the electron/ hole mobility is largely independent of the carrier concentration42. It is thus well justified to approximate the density profile by the measured photoconductivity profile in our diffusion analysis (Fig. 4.2e).

Finally, we briefly discuss the iMIM results at higher illumination intensities. As shown in Fig. 4.16a, b, the temporal evolution of HTL/ETL samples again displays the biexponential decay when PC increases beyond 100 mW/cm^2 (complete data in

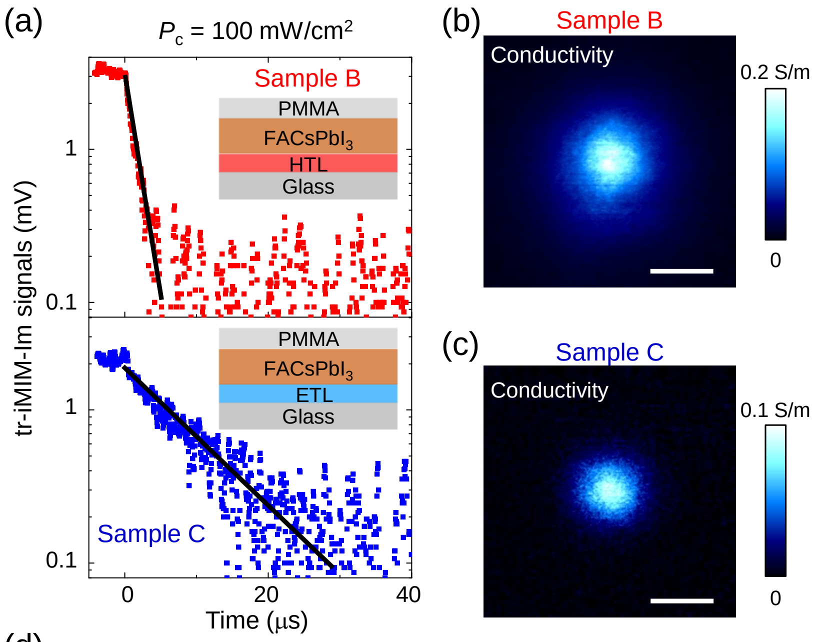

(d)

	L (μm)	τ (μs)	D (cm^2/s)	μ_{diff} (cm^2/V·s)	σ_C (S/m)	n_c, p_c (10^{15} cm^{-3})	μ_{pc} (cm^2/V·s)
Electron (Sample B)	5.2 ±0.7	0.7 ±0.1	0.39 ±0.12	15 ±5	0.16 ±0.02	0.42 ±0.09	24 ±6
Hole (Sample C)	2.7 ±0.6	10 ±2	0.007 ±0.003	0.28 ±0.12	0.06 ±0.01	14 ±5	0.30 ±0.12

Figure 4.11: Results and analysis on HTL/ETL samples. a tr-iMIM signals on the HTL Sample B (upper panel) and ETL Sample C (lower panel). The layer structures of each sample are illustrated in the insets. b Diffusion maps of Sample B and c Sample C under the illumination of 446-nm laser at $P_C = 100$ mW/cm^2. Scale bars are 10 μm. d Tabulated parameters for the calculation of electron/hole mobility values by two methods, i.e., μ_{diff} from the Einstein relation and μ_{pc} from photoconductivity analysis. Panels a-d and captions are from Ref. [4] with permission.

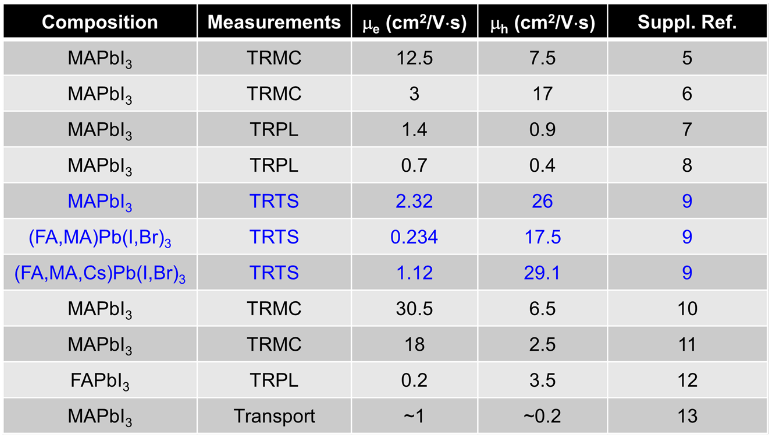

Composition	Measurements	μ_e (cm^2/V·s)	μ_h (cm^2/V·s)	Suppl. Ref.
$MAPbI_3$	TRMC	12.5	7.5	5
$MAPbI_3$	TRMC	3	17	6
$MAPbI_3$	TRPL	1.4	0.9	7
$MAPbI_3$	TRPL	0.7	0.4	8
$MAPbI_3$	TRTS	2.32	26	9
$(FA,MA)Pb(I,Br)_3$	TRTS	0.234	17.5	9
$(FA,MA,Cs)Pb(I,Br)_3$	TRTS	1.12	29.1	9
$MAPbI_3$	TRMC	30.5	6.5	10
$MAPbI_3$	TRMC	18	2.5	11
$FAPbI_3$	TRPL	0.2	3.5	12
$MAPbI_3$	Transport	~1	~0.2	13

Figure 4.12: Tabulated mobility values for MAPI/FAPI thin films. Reference numbers are taken from the list in the main text. Abbreviations: TMRC – Time-resolved microwave conductivity, TRPL – time-resolved photoluminescence, TRTS – time-resolved THz spectroscopy. Panel and caption are from Ref. [4] with permission.

Fig. 4.13), with one of the processes substantially suppressed. For instance, while A1/A2 $\sim$ 2 is expected in plain $FACsPbI_3$, the electron dynamics clearly dominate in Sample B such that $A_1/A_2 > 2$ in Fig. 4.16c. Conversely, with electrons efficiently removed by the ETL, the hole dynamics prevail and $A_1/A_2 < 2$ in Sample C. We have also performed photoconductivity mapping on Samples B and C under various PC (Figs. 4.14 and 4.15) and the results are plotted in Fig. 4.16d. As PC increases towards 10^3-10^4mW/cm^2, the contribution from the other type of carriers is no longer negligible. Consequently, in addition to the general trend of decreasing diffusion length at increasing excitation, L in Sample B decreases further at high P_C, whereas L in Sample C increases slightly at high P_C. Similarly, while only one type of carriers is responsible for the low-power photoconductivity, σ_C does not scale with PC in either sample towards 10^4mW/cm^2 (Fig. 4.16e).

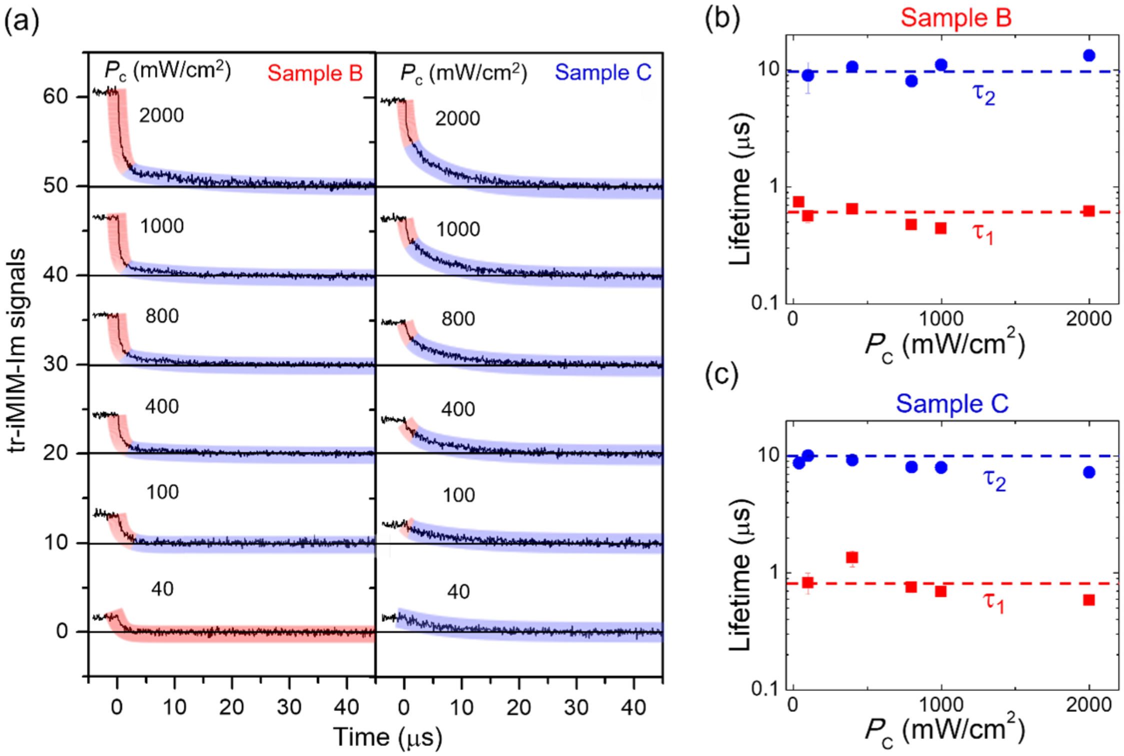

Figure 4.13: Complete tr-iMIM data of sample B and C. (a) Complete tr-iMIM data in linear scale without truncation. The thick lines shaded in red and blue cover the segments of data with fast and slow decays, respectively. (b) Power-dependent lifetimes for Sample B. (c) Power-dependent lifetimes for Sample C. Panels a-c and captions are from Ref. [4] with permission.

4.5 Result Discussion

The spatiotemporally resolved iMIM experiments reveal rich information on organometal trihalide perovskite thin films. To begin with, we take a close look at the impact of GBs on charge transport in PSC materials, which has been under intense debate [40, 59, 63–65]. As summarized in a recent review [66], while GBs strongly affect the current–voltage hysteresis and long-term stability of PSCs, their effect on carrier recombination and thus the open-circuit voltage is rather mild under the illumination of ∼1 Sun. In a previous report[54], we showed that the photoconductivity is spatially homogeneous over grains and GBs, consistent with conductive AFM and SPCM studies [41, 59]. In this work, we further demonstrate that the carrier diffusion is not impeded by the presence of numerous GBs in all three samples. It is possible that the GBs in the current study are not strong nonradiative recombination (i.e., highly defective) centers, and there is no significant band bending at the GBs to block electron/ hole movement across multiple grains [67]. As a result, under the normal solar-cell operation, GBs in our samples do not lead to appreciable spatial variation of transport properties such as the density and mobility of photoexcited carriers, consistent with the early theoretical prediction49. We caution that sample-to-sample variation is widely observed in the PSC research. It is still possible that GBs in other hybrid perovskite thin films exhibit strong impacts on the carrier lifetime and transport properties.

Given the extensive use of PL in studying carrier dynamics, it is instructive to compare the TRPL and tr-iMIM results in our samples. In short, TRPL measured excited states such as exciton recombination via emitted photons, whereas tr-iMIM measures the decay of steady-state conductivity following optical injection of free carriers. In TRPL experiments, the signal strength depends on the radiative recom-

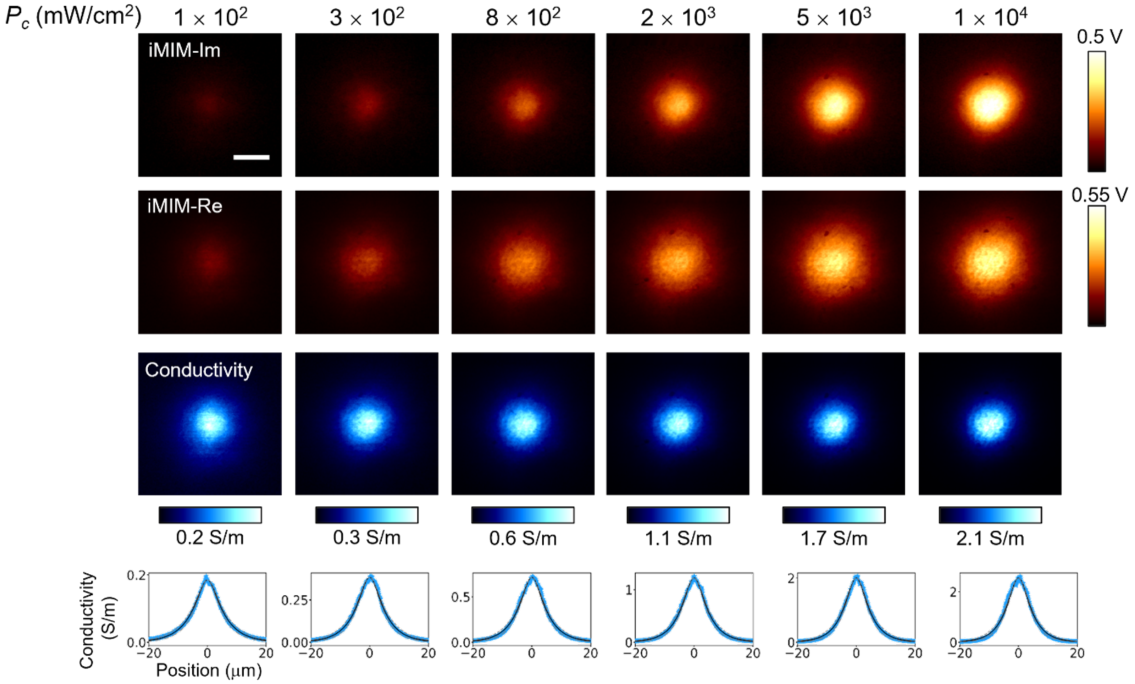

Figure 4.14: Analysis of diffusion images for Sample B. (Top) The raw iMIM-Im, iMIM-Re, and conductivity images. (Bottom) Averaged converted conductivity linecuts for Sample B. Panel and caption are from Ref. [4] with permission.

bination process that emits photons, whereas the temporal evolution measures the total lifetime of certain carriers or excitons [29–31, 39, 40]. For the TRPL data of Sample A in Fig. 4.5b, the fast ($\tau_f \sim 150$ ns) and slow ($\tau_s \sim 0.7$ μs) processes are associated with the surface recombination and the relaxation of the shorter-lived electrons in FACsPbI$_3$, respectively. Note that τ_s matches τ_1 in the tr-iMIM data. After the elapse of τ_s, however, no more mobile electrons are available for radiative recombination with mobile holes. As a result, TRPL cannot measure the lifetime of the longer-lived carriers [37]. We emphasize that the extraction of one type of carriers by HTL or ETL quenches the PL process and the TRPL decay constants in these samples no longer represent lifetimes of electrons or holes in plain PSCs [68]. In triMIM, however, both the signal strength and temporal evolution depend on photoconductivity, which is proportional to the product of carrier density and mobility. For the three time scales above, the decay on the order of 100 ns is not seen in tr-iMIM, presumably due to the small steady-state density and low mobility of surface-bound carriers. On the other hand, because of the low efficiency of radiative recombination in PSCs [37], the removal of free electrons does not lead to appreciable changes in the dynamics of free holes. Consequently, the relaxation process of electrons and holes can be treated independently, as revealed by the tr-iMIM data. It should be noted that PL microscopy has also been utilized to map out the diffusion dynamics in PSC materials [69, 70]. For the same reasons discussed above, it is not straightforward to compare photoluminescence and photoconductivity imaging results across multiple grains, which will be subjected to future experiments.

The difference between photo-physical properties of electrons and holes, as evidenced in Fig. 3d, deserves further discussions. In hybrid perovskites, deep-level defects dominate the trapping/detrapping process and nonradiative recombination of

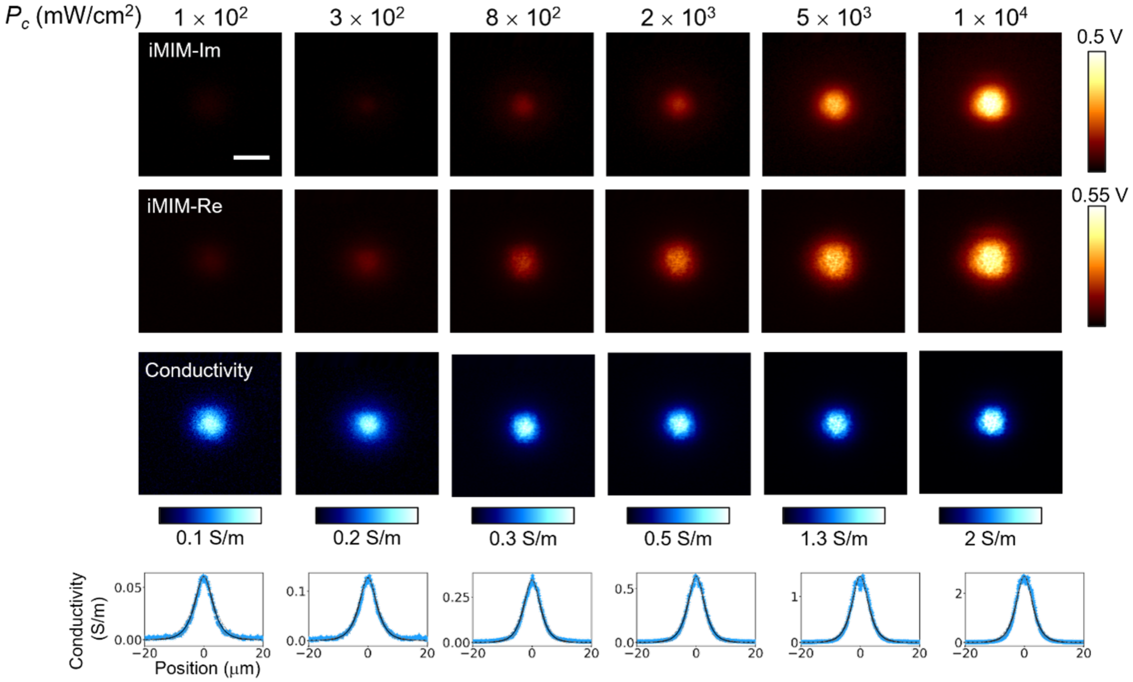

Figure 4.15: Analysis of diffusion images for Sample C. (Top) The raw iMIM-Im, iMIM-Re, and conductivity images. (Bottom) Averaged converted conductivity line-cuts for Sample C. Panel and caption are from Ref. [4] with permission.

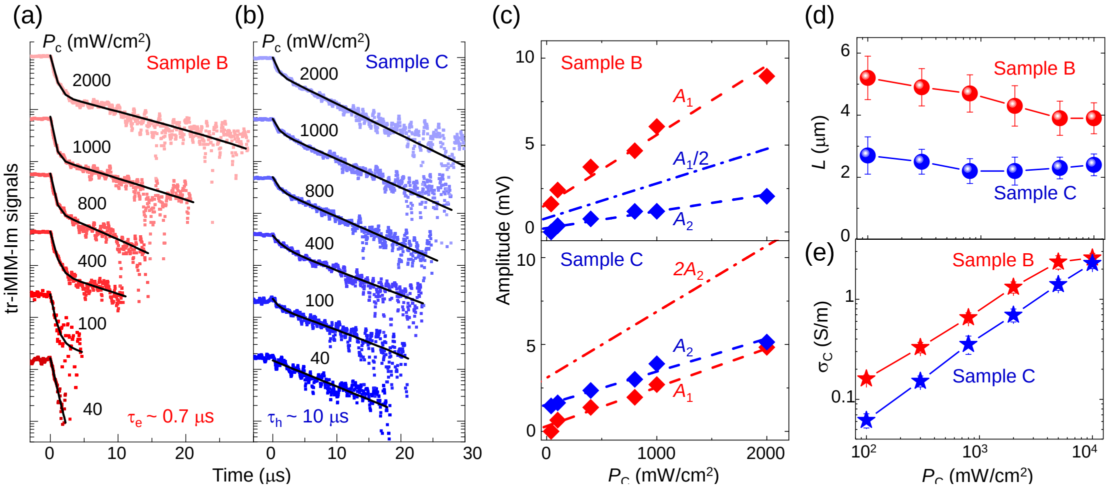

Figure 4.16: Power-dependent iMIM results. (a) tr-iMIM signals on Sample B and (b) Sample C under various laser powers. Signals below the noise level are truncated for clarity. (c) Power-dependent A1 and A2 in Sample B (upper panel) and Sample C (lower panel). The dash-dotted lines are $A_1/2$ (Sample B) and $2A_2$ (Sample C) for comparison with the plain perovskite Sample A, which shows $A_1/A_2 \sim 2$. (d) Power-dependent diffusion lengths and e photoconductivity at the center of the illumination spot in both samples. Panels a-d and captions are from Ref. [4] with permission.

free carriers. In general, the deeper the trap level, the longer time it takes for carriers to be de-trapped, and consequently the longer lifetime and lower mobility. Theoretical studies [71, 72] suggest that cation and anion vacancies create shallow energy levels, while iodine interstitials introduce deep levels in the bandgap. Interestingly, iodine interstitials can be both positively (I_i^+) and negatively (I_i^-) charged, which leads to spatially separated trapped electrons and holes with very low recombination efficiency. The transition energy for I_i^+ (0/+) (de-trapping for electron) is calculated to be 0.48 eV below the conduction band minimum (CBM), whereas the transition energy for I_i^+ (0/-) (de-trapping for hole) is 0.78 eV above the valence band maximum (VBM) [72]. The larger de-trapping barrier for hole results in its longer lifetime and lower mobility. When photoexcited electrons are quenched, the remaining holes will be trapped and then de-trapped via I_i^-, and vice versa. The trapping/de-trapping process induces delayed recombination, as manifested in the tr-iMIM decay curves. This qualitatively explains that the holes have a long carrier lifetime but lower mobility than electrons. Further theoretical work is needed to elucidate this physical picture in a quantitative manner. As a final remark, we emphasize that in solar cells, diffusion lengths of both electrons and holes much larger than the film thickness is desirable for the effective separation of photocarriers. Because of the unique defect properties in hybrid perovskite thin films, as well as the competition between the recombination and trapping/de-trapping process, the imbalance in mobility ($\mu_e \gg \mu_h$) is largely compensated by the imbalance in lifetime ($\tau_e \ll \tau_h$). As a result, the difference between $L_e \sim 5\mu$m and $L_h \sim 3\mu$m is insignificant in our samples, which is of fundamental importance for the superior performance of PSC devices.

In summary, we systematically study the optoelectronic properties of 5%-Cs-doped $FAPbI_3$ thin films (PCE >20%) by imaging the carrier diffusion in real space and detecting the photoconductivity evolution in real time. For plain perovskite films, two relaxation processes are observed on the sample. By selectively removing one type of carriers, we demonstrate that the fast and slow decay constants are associated with the lifetimes of photo-generated electrons and holes, respectively. The diffusion mapping on HTL/ETL samples allows us to extract parameters such as diffusion coefficient, equilibrium carrier density, and mobility of both carriers. The imbalance in carrier lifetime is offset by the difference in mobility such that diffusion lengths of electrons and holes are comparable to each other. We emphasize that, prior to our work, separate experiments are needed to measure relaxation time (TRPL or TRTS) and mobility (transport or SPCM on doped samples) of free carriers. To our knowledge, it is the first time that diffusion length, carrier lifetime, and charge mobility can be individually addressed for mobile electrons and holes on the same batch (as-grown, HTL-coated, and ETLcoated) of samples. The spatiotemporal microwave imaging provides the most direct measurement of photo-physical properties of organometal trihalides, which is crucial for the research and development of these fascinating materials towards commercial products.

Chapter 5: iMIM Spectroscopy of Monolayer Transition Metal Dichalcogenides

We present an innovative, non-invasive optical-pump-electrical-probe characterization instrument, the Illuminated Microwave Impedance Microscopy Spectroscopy (iMIM Spectroscopy). This apparatus offers both illumination wavelength sweeping and time-resolving capabilities to explore the static and dynamic properties of excitons in materials. Our research applies iMIM spectroscopy to two-dimensional semiconductors, specifically the monolayer transition metal dichalcogenides (TMDs) materials WSe_2 and WS_2 which are known for their tightly bound excitons and pronounced light-matter interactions. Through our experimentation, we identified excitonic peaks in the iMIM spectra, ascribed to optical absorption and the modulation of local conductance via defect-mediated exciton dissociation. Interestingly, our data show that the carrier lifetimes remained consistent across different wavelengths. Moreover, we observed blueshifts of excitonic peaks at low temperatures, signifying alterations in exciton binding energies. These results showcase the potential of iMIM spectroscopy to reveal the rich excitonic physics of monolayer TMDs.

This is an ongoing project and may need further investigation before submitting to the journal.

5.1 Introduction

Excitons are bound electron-hole pairs that play a crucial role in the optical and electronic properties of semiconductors. In monolayer transition metal dichalcogenides (TMDs) such as tungsten diselenide (WSe_2) and tungsten disulfide (WS_2), excitons are particularly prominent due to the reduced screening and enhanced Coulomb interaction in two dimensions. [73–76] These materials exhibit strong light-matter interaction and rich exciton physics, such as spin-valley locking, exciton-exciton annihilation, and many-body effects. [77] Moreover, monolayer TMDs have direct bandgaps at the corners of the Brillouin zone (K and K' points), which enable efficient optical transitions between the spin-split valence and conduction bands. [7] These features make monolayer TMDs attractive candidates for optoelectronic and spin-valleytronic applications. [78]

Various approaches have been employed to study the exciton physics in monolayer TMDs, such as photoluminescence (PL) [77, 79–82], optical absorption [77, 81, 83, 84], photocurrent measurements [85–87], etc. These methods have their advantages, but also some limitations. For example, photoluminescence can probe the optical transitions, but not the local conductivity of the material, thus lacking an essential electrical perspective. [80] Optical absorption, while capable of providing information on the energy structure of the material, is sensitive to the environment and may not provide local spatial information about the material's electronic properties. [84] Photocurrent measurements require specific device designs to achieve extrinsic exciton dissociation and invasively deposit electrodes on the sample, which may affect the intrinsic properties of the material. [87]

In this work, we introduce a novel characterization tool for excitonic physics studies: light-illuminated Microwave Impedance Microscopy Spectroscopy (iMIM Spectroscopy), a unique optical-pump-electrical-probe technique with 1-nm spectral resolution, in addition to iMIM's 10-ns temporal resolution and 20-nm spatial resolution, for electrical probing without the need for external contacts or electrodes. [3, 4, 48, 88] Leveraging the integration of iMIM technology with the energy resolving capabilities of the supercontinuum laser and monochromator, our iMIM Spectroscopy methodology collects MIM signals across varying illumination wavelengths, or photon energies. This process generates an iMIM spectrum that offers valuable insight into the exciton dynamics of the materials under investigation. Arguably, excitons dissociating into free carriers with the help of trap states induced by defects or impurities can modulate the local conductance of the material [89–91], which thus can be detected by MIM electronics.

We have utilized iMIM spectroscopy on monolayer WSe_2 and WS_2 samples, and observed distinct excitonic peaks within their iMIM spectra. These peaks exhibit remarkable resolution and align extrememly well with the respective photoluminescence (PL) peaks, underscoring the proficiency of iMIM Spectroscopy in accurately discerning features of exciton dissociation in monolayer TMDs. Additionally, we reveal that the peaks discerned via iMIM spectroscopy exhibit a blueshift at lower temperatures, lending further credence to the veracity of the observed excitonic features. Our observations affirm that iMIM spectroscopy serves as a potent, non-invasive technique for exploring the interplay between the optical and electrical properties of monolayer TMDs at the nanoscale. Specifically, these results demonstrate the power of iMIM spectroscopy for studying the exciton physics in 2D semiconductors and reveal new insights into the optical and electronic properties of monolayer TMDs.

5.2 Experiment Results

We prepared monolayer WSe_2 and WS_2 samples by mechanical exfoliation, transfer and stacking of the layers on thin layer hBNs. The substrate was a transparent double-polished sapphire, which allowed MIM tip and laser input to position at opposite sides of the substrate while aligned. The optical images of the samples are

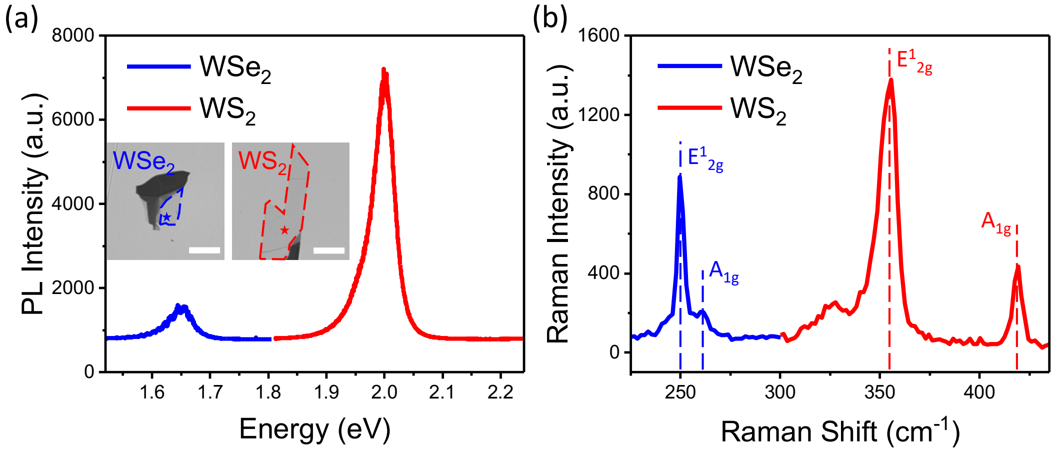

Figure 5.1: Photoluminescence (PL) and Raman of WSe_2 and WS_2. Scale bars represent 20μm. (a) PL spectra. Insets are optical images of WSe_2 and WS_2 samples with enclosed monolayer regions and starred measurement positions. Scale bars represent a length of 20μm. (b) Raman spectra. In-plane E_{2g}^1 mode and the out-of-plane A_{1g} mode for WSe_2 and WS_2 are labeled correspondingly.

shown in the insets of Figure 5.1a.

We performed conventional characterization of the samples by PL and Raman. The PL spectra of WSe_2 and WS_2 show their peaks at 1.65 eV and 2.0 eV, respectively, as shown in Figure 5.1a. These peaks correspond to the excitonic transitions in the monolayers and will be later compared with the iMIM spectroscopy peaks. The Raman spectra of WSe_2 and WS_2 show the characteristic peaks of monolayer TMDs, such as the in-plane E2g mode and the out-of-plane A1g mode, as shown in Figure 5.1b.

In iMIM Spectroscopy measurements, we employed microwave impedance microscopy (MIM) to measure the local conductance of the samples under laser illumination. MIM is a scanning probe technique that probes local conductivity and permittivity by measuring the admittance between a sharp tip and the sample at microwave frequencies. The admittance is composed of a real part (conductance)

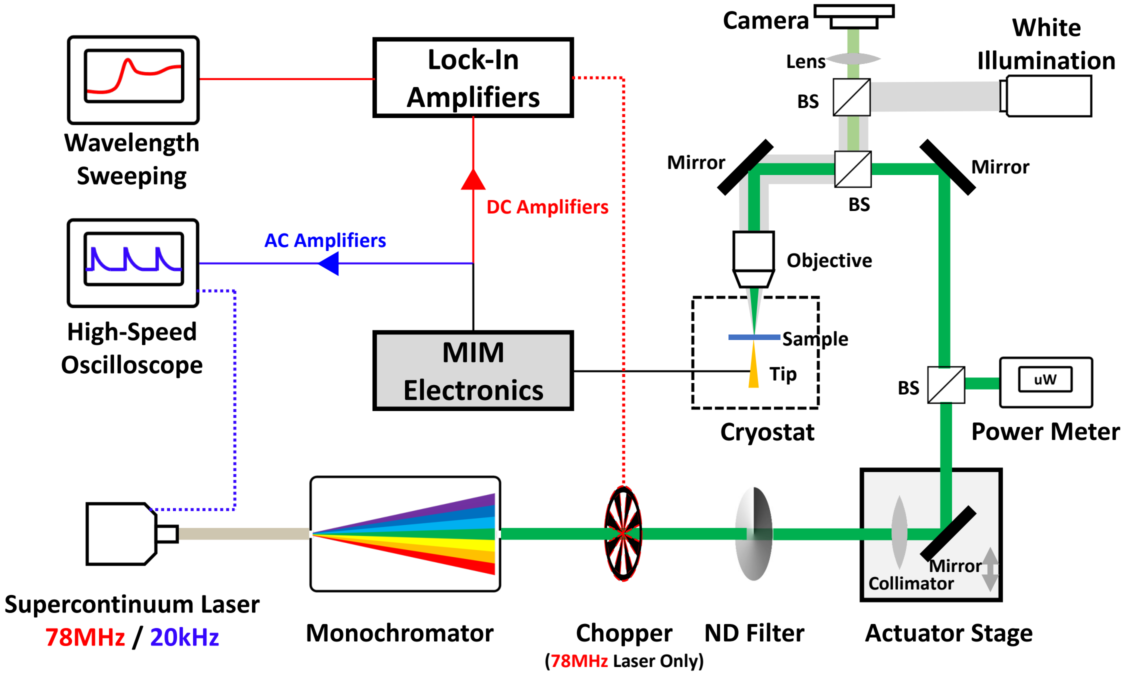

Figure 5.2: Schematic of iMIM spectroscopy system. Red fonts and lines are for the wavelength sweeping configuration with the 78MHz quasi-CW white laser source. Blue fonts and lines are for the time-resolved configuration with the 20kHz white laser source.

and an imaginary part (capacitance), which can be converted from the MIM signals (MIM real part and MIM imaginary part) based on finite element analysis (FEA) simulations in Figure 5.4.

The instrumentation of iMIM spectroscopy, as illustrated in Figure 5.2, utilizes several essential components. We used a SuperK Fianium supercontinuum laser (78 MHz) as our laser source. The laser's wavelength was selected via a monochromator. An optical chopper was employed for demodulation. To calibrate the laser's intensity, we made use of a neutral density (ND) filter. Additionally, we implemented an actuator stage equipped with a collimator and mirror on a motorized stage, which was primarily to compensate for laser path drift arising from wavelength changes in

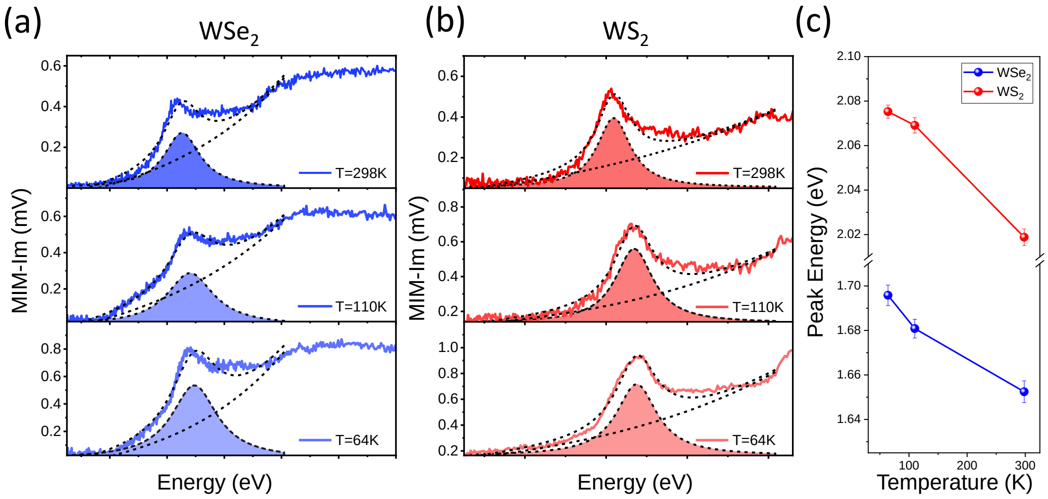

Figure 5.3: iMIM spectra of WSe_2 and WS_2 at room and low temperatures. (a) MIM-Im signals of WSe_2 under different temperatures. (b) MIM-Im signals of WS_2 under different temperatures. (c) Exciton peak energies of WSe_2 and WS_2 under different temperatures.

the monochromator grating, as shown in Figure 3.7. A dedicated optical system was implemented with mirrors, objectives, and beam splitters to direct the laser into the cryostat from the top and measure the power simultaneously. The system included a cryostat for creating a low-temperature high vacuum environment, which contained a piezo stack for controlling the sample position. The MIM tip cantilever in the cryostat gathered MIM signals from the tip-sample interaction area and sends the signals to MIM electronics for data gathering and processing.

Figure 5.3 illustrates the iMIM spectra for WSe_2 and WS_2 at both room temperature and lower temperatures. We fitted each spectrum with a Gaussian function for the peak and an exponential function for the background, which accounts for the Urbach tail of the direct interband absorption edge. [86, 92] The sum of these two

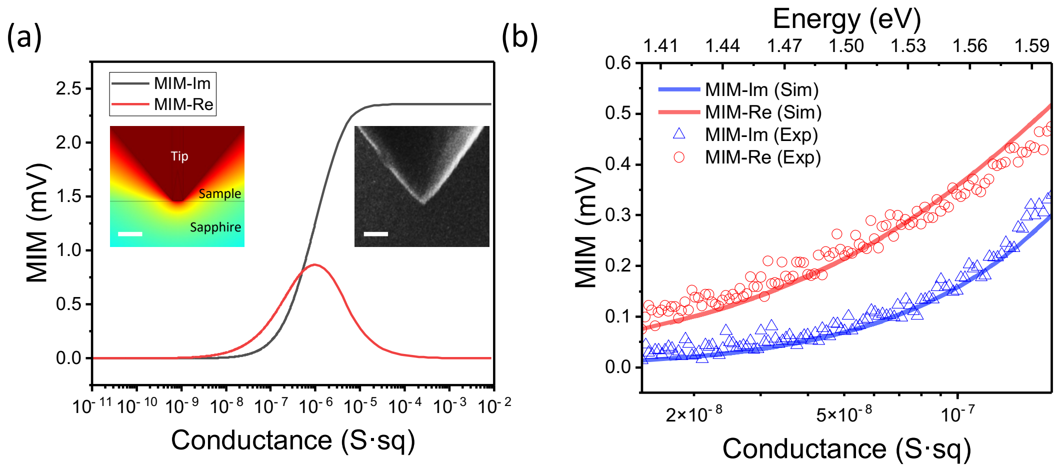

Figure 5.4: Tip-sample FEA simulation and fitting with real data. (a) Comsol FEA simulation results based on the real tip profile as shown in the inset by SEM. (b) Comparison example of experimental data (WSe_2 at 298K) and simulation curves.

functions delivered a satisfactory fit to the overall spectral shape. Specifically, Figure 3a displays the MIM signals as a function of photon energy (ranging from 1.25 eV to 2.4 eV) for WSe_2 at different temperatures. Similarly, Figure 3b depicts the MIM signals as a function of photon energy (from 1.65 eV to 2.45 eV) for WS_2 at the same two temperatures. Figure 5.3c provides a summary of the changes in exciton peak energy as a function of temperature. WS_2 exhibits an exciton peak shift from 2.019 eV at T=298 K to 2.069 eV at T=110 K, and 2.075 eV at T=64 K, while WSe_2 shows a similar shift from 1.652 eV at T=298 K to 1.681 eV at T=110 K and 1.696 eV at T=64 K.

In order to measure carrier lifetimes, which can extend to the order of ns, μs and beyond, we substituted the 78 MHz (with a 13 ns period) laser with the 20 kHz (with a 50 μs period) SuperK Compact supercontinuum laser and removed the optical chopper. A high-speed oscilloscope reader was employed to capture the decay curves of iMIM-Im signals following each laser pulse as shown in Figure 5.2. Given that the

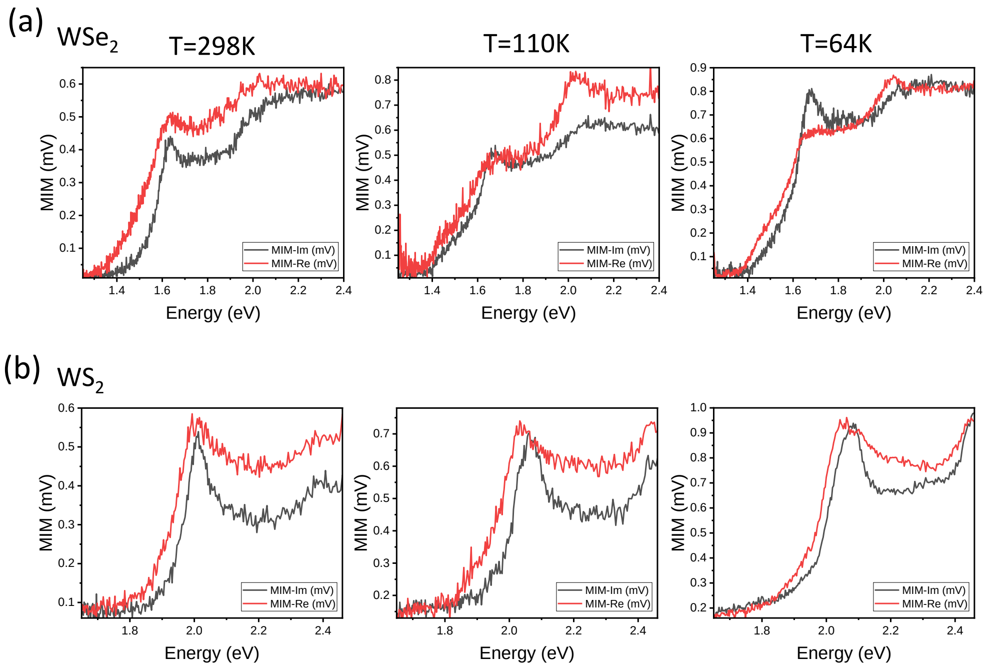

Figure 5.5: MIM-Im and MIM-Re data under different temperatures. Inset a for WSe$_2$ and b for WS$_2$.

iMIM-Im signal approximately scales with photo conductance within our measurement range, as indicated in Figure 5.4, we will directly use the raw MIM data without conductance conversion for the subsequent analysis. To accommodate the presence of two distinct carrier lifetimes, the decay curves were fitted using biexponential function $y = A_1 e^{-t/\tau_1} + A_2 e^{-t/\tau_2}$. Figure 5.6a provides an example of iMIM-Im decays for WSe$_2$ for different photon energies, and Figure 5.6b is the iMIM-Im decay for WSe$_2$ at around their exciton energies, along with its fitted curves under room temperature. Figure 5.6c presents a statistical analysis of the WSe$_2$ lifetimes for different photon energies ranging from 1.6 eV to 2.4 eV which do not show significant variation, with the average lifetimes from the fittings equating to 19 ns and 1639 ns. Figures 5.6d-f offer similar findings for WS$_2$ at wavelengths from 1.9 eV to 2.4 eV, with the two measured lifetimes being 62 ns and 1501 ns. It is important to note that the photon

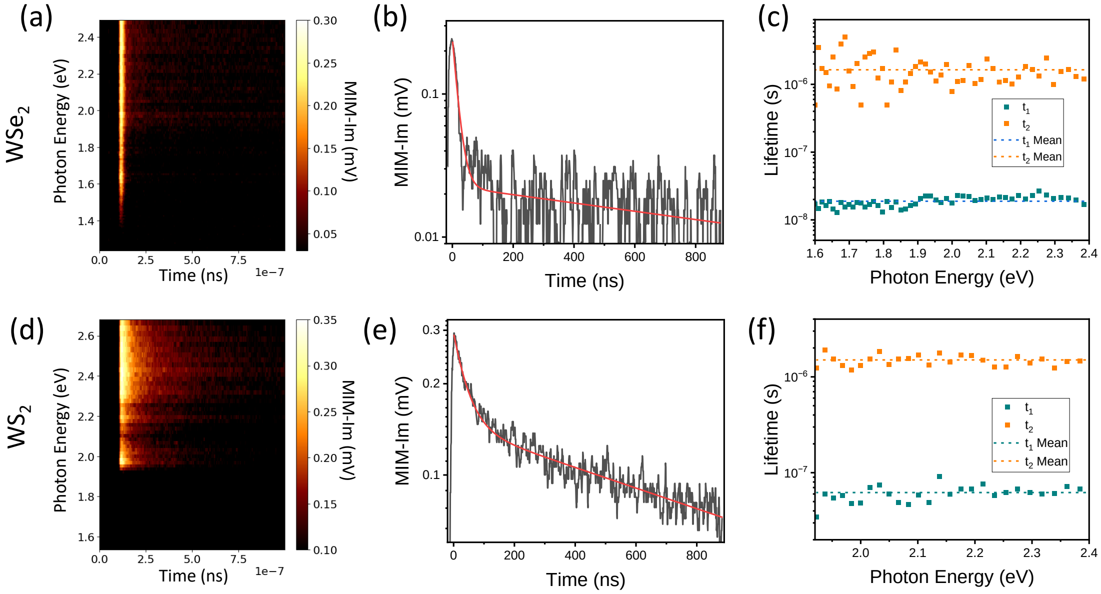

Figure 5.6: Carrier lifetimes of WSe_2 and WS_2 at different wavelengths. Insets a and d are iMIM-Im decay heatmaps for different photon energies of WSe_2 and WS_2. Insets b and e are iMIM-Im decay signals and fitted curves near the exciton energies of WSe_2 and WS_2 respectively. Insets c and f are statistics of carriers lifetimes of WSe_2 and WS_2.

energy ranges presented in Figure 5.6c,f are narrower than those in Figure 5.3. This is because lower-signal energies are not capable of producing high signal-to-noise ratio decay curves suitable for appropriate fittings.

5.3 Discussion

Our experimental results have showcased iMIM spectroscopy as a novel tool for studying exciton physics in transition metal dichalcogenides (TMDs). This technique combines the benefits of optical and electrical methods, enabling high resolution examination of the excitonic properties of monolayer WSe_2 and WS_2. We will now discuss the implications of our findings and draw comparisons with prior studies.

Exciton detection predominantly relies on two methodologies: optical and

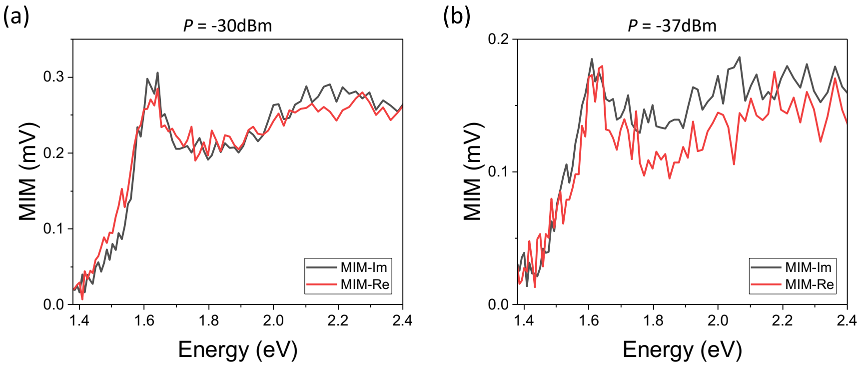

Figure 5.7: MIM signals of WSe_2 at -30dBm and -37dBm tip powers.

electrical. A range of optical techniques has been developed, including photoluminescence, absorption, reflectance, and photo-reflectance spectroscopy, etc. [77, 93–95] However, these methods can face limitations, such as cases with a low photoluminescence yield (<1%) presumably due to defect trap states. [93] Moreover, only a subset of incoherent excitons positioned within the light cone, possessing a zero center-of-mass momentum, can undergo decay via radiative recombination. [93] Electrical techniques on the other hand, like photocurrent spectroscopy, fundamentally collect electric rather than optical responses and offer certain advantages, including high spatial resolution and reduced susceptibility to optical interference effects. Nevertheless, they require invasive contacts or electrodes on the sample and depend on long-distance transport properties. iMIM spectroscopy method offers a fresh perspective on exciton physics in 2D semiconductors. It integrates the strengths of MIM and optical excitation, allowing for the probing of 2D materials' optoelectrical responses without necessitating external contacts or electrodes.

Arguably, the mechanism of iMIM spectroscopy is based on the dissociation of excitons by defects in the TMDs. Defects can act as charge traps that capture either electrons or holes from excitons, leaving behind free carriers that contribute to the conductivity, while the defect density and type can vary depending on the synthesis method and treatment of the TMDs. [48, 89–91, 96] It is important to distinguish the dissociation of excitons with defect trap states from the dissociation potentially caused by MIM measurements. In MIM measurements, a high-frequency 1GHz voltage is applied to a sharp metallic tip scanning the sample surface. However, theoretical calculations suggest that the electric field generated by typical MIM tip power (-20dBm) is not adequate to break up excitons in monolayer TMDs. [48, 97, 98] This observation is further supported when we reduce the tip power to -30dBm and -37dBm, and yet continue to observe both MIM imaginary and real signals, along with distinct excitonic features (as shown in Figure 5.7). Also, the coexistence of imaginary and real signals hints that the exciton response mainly comes from conductance change, compared to possible dipole oscillation which does not increase carrier density and should not be observed in the real part. [3, 98] Consequently, we attribute the iMIM signal predominantly to defect-mediated dissociation. Nevertheless, we cannot entirely discount the potential contribution of exciton dipoles to the dielectric properties, which may in turn influence MIM signals in the observations under consideration. Future investigations are required for further validation.

Interestingly and surprisingly, we find that the excitonic peaks blueshift with lower temperatures, as shown in Figure 5.3c. This phenomenon is similar to what has been observed in PL measurements for monolayer TMDs. The blueshift of exciton peaks are usually explained by the reduction of thermal expansion effect and electron-phonon interaction, which increases the energy of the exciton peak at lower temperatures. [99–103] The blueshift of exciton peaks further confirms the validity of our iMIM spectroscopy method to characterize exciton physics in 2D semiconductors.

Our lifetime measurements reveal some interesting patterns. Lifetimes of WS_2

are generally longer than those of WSe_2, consistent with previous reports. [48, 89] Also, the lifetime does not significantly change with the wavelength of the incident light within the given ranges. This suggests that the recombination process in these materials is relatively insensitive to the initial excitation energy.

5.4 Conclusion

In summary, we have presented iMIM spectroscopy, a novel characterization tool for 2D semiconductors, which combines the advantages of MIM and optical excitation. We have applied this tool to monolayer WSe_2 and WS_2 samples and observed excitonic peaks, carrier dynamics, and blueshifts of excitonic peaks in low temperatures. We believe that our iMIM spectroscopy method can provide new insights into the exciton physics in 2D semiconductors and enable new applications in photonics and optoelectronics.

Chapter 6: Summary and Outlook

Throughout this dissertation, I have detailed the fundamental operation principles of microwave impedance microscopy (MIM) and its optically coupled mode, illuminated MIM (iMIM). I have outlined the diverse functionalities of iMIM, which include carrier diffusion measurements, lifetime dynamics analysis, and spectroscopy investigations.

A significant portion of the discussion was dedicated to my part of contribution to the construction of the time-resolved iMIM system, and the recounting of my design, assembly, and application of the iMIM spectroscopy system, highlighting its value and the central role it played in the studies.

The unique capabilities of the iMIM spectroscopy system were demonstrated through two discussed studies involving specific materials. These investigations underscored our unparalleled ability to investigate carrier and excitonic physics with exceptional spatial, temporal, and spectral resolutions.

Nevertheless, our work extends beyond these achievements in instrumentation and physics. The comprehensive iMIM toolset we have developed paves the way for numerous potential projects. For instance, by gating TMD monolayers, we anticipate the generation of an increased number of trions, which our method is perfectly suited to observe and study. The metallic nature of the probe allows us to consider the possibility of using the tip as a top gate with a specific DC voltage. This prospect could simplify sample preparation requirements significantly.

Moreover, fascinating structures like twisted homo-bilayer or heterostructures provide an opportunity to delve into the dynamics of excitons and carriers in moiré systems. This can be achieved by exploring various twist angles and coupling mechanisms, focusing on aspects such as diffusion lengths, lifetimes, and exciton peaks.

While TMDs and perovskites have been central to our investigations, our fs-supercontinuum laser can also be leveraged in studies of photo-induced metal-insulator transitions, such as the charge density wave (CDW) state of 1T-TaS2 [104–106].

At the time of writing this dissertation, we are actively refining the iMIM system and engaging in collaborative work with other researchers. We firmly believe that the continuation of this work will substantially contribute to both the fields of microwave impedance microscopy and photoresponse research.

Bibliography

[1] Yuanyuan Zhou, Laura M. Herz, Alex K-Y Jen, and Michael Saliba. Advances and challenges in understanding the microscopic structure-property-performance relationship in perovskite solar cells. *NATURE ENERGY*, 7(9):794–807, SEP 2022.

[2] Gang Wang, Alexey Chernikov, Mikhail M. Glazov, Tony F. Heinz, Xavier Marie, Thierry Amand, and Bernhard Urbaszek. Colloquium: Excitons in atomically thin transition metal dichalcogenides. *REVIEWS OF MODERN PHYSICS*, 90(2), APR 4 2018.

[3] Zhaodong Chu, Lu Zheng, and Keji Lai. Microwave microscopy and its applications. In DR Clarke, editor, *ANNUAL REVIEW OF MATERIALS RESEARCH, VOL 50, 2020*, volume 50 of *Annual Review of Materials Research*, pages 105–130. 2020.

[4] Xuejian Ma, Fei Zhang, Zhaodong Chu, Ji Hao, Xihan Chen, Jiamin Quan, Zhiyuan Huang, Xiaoming Wang, Xiaoqin Li, Yanfa Yan, Kai Zhu, and Keji Lai. Superior photo-carrier diffusion dynamics in organic-inorganic hybrid perovskites revealed by spatiotemporal conductivity imaging. *NATURE COMMUNICATIONS*, 12(1), AUG 18 2021.

[5] Shida Yang, Weifei Fu, Zhongqiang Zhang, Hongzheng Chen, and Chang-Zhi Li. Recent advances in perovskite solar cells: efficiency, stability and lead-free perovskite. *JOURNAL OF MATERIALS CHEMISTRY A*, 5(23):11462–11482, JUN 21 2017.

[6] Abdulaziz S. R. Bati, Yu Lin Zhong, Paul L. Burn, Mohammad Khaja Nazeeruddin, Paul E. Shaw, and Munkhbayar Batmunkh. Next-generation applications for integrated perovskite solar cells. *COMMUNICATIONS MATERIALS*, 4(1), JAN 5 2023.

[7] Kin Fai Mak, Changgu Lee, James Hone, Jie Shan, and Tony F. Heinz. Atomically thin MoS2: A new direct-gap semiconductor. *PHYSICAL REVIEW LETTERS*, 105(13), SEP 24 2010.

[8] Di Xiao, Gui-Bin Liu, Wanxiang Feng, Xiaodong Xu, and Wang Yao. Coupled spin and valley physics in monolayers of MoS2 and other group-vi dichalcogenides. *PHYSICAL REVIEW LETTERS*, 108(19), MAY 7 2012.

[9] Hualing Zeng and Xiaodong Cui. An optical spectroscopic study on two-dimensional group-vi transition metal dichalcogenides. *CHEMICAL SOCIETY REVIEWS*, 44(9):2629–2642, 2015.

[10] Kin Fai Mak and Jie Shan. Photonics and optoelectronics of 2d semiconductor transition metal dichalcogenides. *NATURE PHOTONICS*, 10(4):216–226, APR 2016.

[11] A. H. Castro Neto, F. Guinea, N. M. R. Peres, K. S. Novoselov, and A. K. Geim. The electronic properties of graphene. *REVIEWS OF MODERN PHYSICS*, 81(1):109–162, JAN-MAR 2009.

[12] A. Chaves, J. G. Azadani, Hussain Alsalman, D. R. da Costa, R. Frisenda, A. J. Chaves, Seung Hyun Song, Y. D. Kim, Daowei He, Jiadong Zhou, A. Castellanos-Gomez, F. M. Peeters, Zheng Liu, C. L. Hinkle, Sang-Hyun Oh, Peide D. Ye, Steven J. Koester, Young Hee Lee, Ph. Avouris, Xinran Wang, and Tony Low.

Bandgap engineering of two-dimensional semiconductor materials. *NPJ 2D MATERIALS AND APPLICATIONS*, 4(1), AUG 24 2020.

[13] Zhiwei Peng, Xiaolin Chen, Yulong Fan, David J. Srolovitz, and Dangyuan Lei. Strain engineering of 2d semiconductors and graphene: from strain fields to band-structure tuning and photonic applications. *LIGHT-SCIENCE & APPLICATIONS*, 9(1), DEC 23 2020.

[14] Jonas Gael Roch, Guillaume Froehlicher, Nadine Leisgang, Peter Makk, Kenji Watanabe, Takashi Taniguchi, and Richard John Warburton. Spin-polarized electrons in monolayer MoS2. *NATURE NANOTECHNOLOGY*, 14(5):432–436, MAY 2019.

[15] Patrick Back, Meinrad Sidler, Ovidiu Cotlet, Ajit Srivastava, Naotomo Takemura, Martin Kroner, and Atac Imamoglu. Giant paramagnetism-induced valley polarization of electrons in charge-tunable monolayer MoSe2. *PHYSICAL REVIEW LETTERS*, 118(23), JUN 9 2017.

[16] Hualing Zeng, Junfeng Dai, Wang Yao, Di Xiao, and Xiaodong Cui. Valley polarization in MoS2 monolayers by optical pumping. *NATURE NANOTECHNOLOGY*, 7(8):490–493, AUG 2012.

[17] G. Sallen, L. Bouet, X. Marie, G. Wang, C. R. Zhu, W. P. Han, Y. Lu, P. H. Tan, T. Amand, B. L. Liu, and B. Urbaszek. Robust optical emission polarization in MoS2 monolayers through selective valley excitation. *PHYSICAL REVIEW B*, 86(8), AUG 6 2012.

[18] Kha Tran, Galan Moody, Fengcheng Wu, Xiaobo Lu, Junho Choi, Kyounghwan Kim, Amritesh Rai, Daniel A. Sanchez, Jiamin Quan, Akshay Singh, Jacob

Embley, Andre Zepeda, Marshall Campbell, Travis Autry, Takashi Taniguchi, Kenji Watanabe, Nanshu Lu, Sanjay K. Banerjee, Kevin L. Silverman, Suenne Kim, Emanuel Tutuc, Li Yang, Allan H. MacDonald, and Xiaoqin Li. Evidence for moiré excitons in van der waals heterostructures. *NATURE*, 567(7746):71+, MAR 7 2019.

[19] Di Huang, Junho Choi, Chih-Kang Shih, and Xiaoqin Li. Excitons in semiconductor moiré superlattices. *NATURE NANOTECHNOLOGY*, 17(3):227–238, MAR 2022.

[20] Dong Seob Kim, Roy C. Dominguez, Rigo Mayorga-Luna, Dingyi Ye, Jacob Embley, Tixuan Tan, Yue Ni, Zhida Liu, Mitchell Ford, Frank Y. Gao, Saba Arash, Kenji Watanabe, Takashi Taniguchi, Suenne Kim, Chih-Kang Shih, Keji Lai, Wang Yao, Li Yang, Xiaoqin Li, and Yoichi Miyahara. Electrostatic moiré potential from twisted hexagonal boron nitride layers. *NATURE MATERIALS*, AUG 2023.

[21] Y.-T. Cui and E. Yue Ma. Microwave impedance microscopy. *Capacitance Spectroscopy of Semiconductors*, page 411–435, 2018.

[22] Martin A. Green, Anita Ho-Baillie, and Henry J. Snaith. The emergence of perovskite solar cells. *NATURE PHOTONICS*, 8(7):506–514, JUL 2014.

[23] Nam-Gyu Park. Perovskite solar cells: an emerging photovoltaic technology. *MATERIALS TODAY*, 18(2):65–72, MAR 2015.

[24] Zhen Li, Talysa R. Klein, Dong Hoe Kim, Mengjin Yang, Joseph J. Berry, Maikel F. A. M. van Hest, and Kai Zhu. Scalable fabrication of perovskite solar cells. *NATURE REVIEWS MATERIALS*, 3(4), APR 2018.

[25] NREL. Best research-cell efficiency chart. 2020.

[26] Stefaan De Wolf, Jakub Holovsky, Soo-Jin Moon, Philipp Loeper, Bjoern Niesen, Martin Ledinsky, Franz-Josef Haug, Jun-Ho Yum, and Christophe Ballif. Organometallic halide perovskites: Sharp optical absorption edge and its relation to photovoltaic performance. *JOURNAL OF PHYSICAL CHEMISTRY LETTERS*, 5(6):1035–1039, MAR 20 2014.

[27] Carlito S. Ponseca, Jr., Tom J. Savenije, Mohamed Abdellah, Kaibo Zheng, Arkady Yartsev, Tobjorn Pascher, Tobias Harlang, Pavel Chabera, Tonu Pullerits, Andrey Stepanov, Jean-Pierre Wolf, and Villy Sundstrom. Organometal halide perovskite solar cell materials rationalized: Ultrafast charge generation, high and microsecond-long balanced mobilities, and slow recombination. *JOURNAL OF THE AMERICAN CHEMICAL SOCIETY*, 136(14):5189–5192, APR 9 2014.

[28] Hikaru Oga, Akinori Saeki, Yuhei Ogomi, Shuzi Hayase, and Shu Seki. Improved understanding of the electronic and energetic landscapes of perovskite solar cells: High local charge carrier mobility, reduced recombination, and extremely shallow traps. *JOURNAL OF THE AMERICAN CHEMICAL SOCIETY*, 136(39):13818–13825, OCT 1 2014.

[29] Dong Shi, Valerio Adinolfi, Riccardo Comin, Mingjian Yuan, Erkki Alarousu, Andrei Buin, Yin Chen, Sjoerd Hoogland, Alexander Rothenberger, Khabiboulakh Katsiev, Yaroslav Losovyj, Xin Zhang, Peter A. Dowben, Omar F. Mohammed, Edward H. Sargent, and Osman M. Bakr. Low trap-state density and long carrier diffusion in organolead trihalide perovskite single crystals. *SCIENCE*, 347(6221):519–522, JAN 30 2015.

[30] Samuel D. Stranks, Giles E. Eperon, Giulia Grancini, Christopher Menelaou, Marcelo J. P. Alcocer, Tomas Leijtens, Laura M. Herz, Annamaria Petrozza, and Henry J. Snaith. Electron-hole diffusion lengths exceeding 1 micrometer in an organometal trihalide perovskite absorber. *SCIENCE*, 342(6156):341–344, OCT 18 2013.

[31] Guichuan Xing, Nripan Mathews, Shuangyong Sun, Swee Sien Lim, Yeng Ming Lam, Michael Graetzel, Subodh Mhaisalkar, and Tze Chien Sum. Long-range balanced electron- and hole-transport lengths in organic-inorganic. *SCIENCE*, 342(6156):344–347, OCT 18 2013.

[32] Jingyu Qian, Bin Xu, and Wenjing Tian. A comprehensive theoretical study of halide perovskites ABX(3). *ORGANIC ELECTRONICS*, 37:61–73, OCT 2016.

[33] Samuel Ponce, Martin Schlipf, and Feliciano Giustino. Origin of low carrier mobilities in halide perovskites. *ACS ENERGY LETTERS*, 4(2):456–463, FEB 2019.

[34] Sandip R. Kumavat, Yogesh Sonvane, Deobrat Singh, and Sanjeev K. Gupta. Two-dimensional with high efficiency and superior carrier mobility: A theoretical study. *JOURNAL OF PHYSICAL CHEMISTRY C*, 123(9):5231–5239, MAR 7 2019.

[35] Laura M. Herz. Charge-carrier mobilities in metal halide perovskites: Fundamental mechanisms and limits. *ACS ENERGY LETTERS*, 2(7):1539–1548, JUL 2017.

[36] Eran Edri, Saar Kirmayer, Alex Henning, Sabyasachi Mukhopadhyay, Konstantin Gartsman, Yossi Rosenwaks, Gary Hodes, and David Cahen. Why lead methylammonium tri-iodide perovskite-based solar cells require a mesoporous electron transporting scaffold (but not necessarily a hole conductor). *NANO LETTERS*, 14(2):1000–1004, FEB 2014.

[37] Giselle A. Elbaz, Daniel B. Straus, Octavi E. Semonin, Trevor D. Hull, Daniel W. Paley, Philip Kim, Jonathan S. Owen, Cherie R. Kagan, and Xavier Roy. Unbalanced hole and electron diffusion in lead bromide perovskites. *NANO LETTERS*, 17(3):1727–1732, MAR 2017.

[38] Yaxin Zhai, Kang Wang, Fei Zhang, Chuanxiao Xiao, Aaron H. Rose, Kai Zhu, and Matthew C. Beard. Individual electron and hole mobilities in lead-halide perovskites revealed by noncontact methods. *ACS ENERGY LETTERS*, 5(1):47–55, JAN 2020.

[39] Yasuhiro Yamada, Toru Nakamura, Masaru Endo, Atsushi Wakamiya, and Yoshihiko Kanemitsu. Photocarrier recombination dynamics in perovskite CH3NH3PbI3 for solar cell applications. *JOURNAL OF THE AMERICAN CHEMICAL SOCIETY*, 136(33):11610–11613, AUG 20 2014.

[40] Dane W. deQuilettes, Sarah M. Vorpahl, Samuel D. Stranks, Hirokazu Nagaoka, Giles E. Eperon, Mark E. Ziffer, Henry J. Snaith, and David S. Ginger. Impact of microstructure on local carrier lifetime in perovskite solar cells. *SCIENCE*, 348(6235):683–686, MAY 8 2015.

[41] Shuhao Liu, Lili Wang, Wei-Chun Lin, Sukrit Sucharitakul, Clemens Burda, and Xuan P. A. Gao. Imaging the long transport lengths of photo-generated

carriers in oriented perovskite films. *NANO LETTERS*, 16(12):7925–7929, DEC 2016.

[42] Zhenxuan Zhao, Xiangyu Chen, Huaqiang Wu, Xiaoming Wu, and Guozhong Cao. Probing the photovoltage and photocurrent in perovskite solar cells with nanoscale resolution. *ADVANCED FUNCTIONAL MATERIALS*, 26(18):3048–3058, MAY 10 2016.

[43] Arianna Marchioro, Joel Teuscher, Dennis Friedrich, Marinus Kunst, Roel van de Krol, Thomas Moehl, Michael Graetzel, and Jacques-E Moser. Unravelling the mechanism of photoinduced charge transfer processes in lead iodide perovskite solar cells. *NATURE PHOTONICS*, 8(3):250–255, MAR 2014.

[44] Eline M. Hutter, Jan-Jaap Hofman, Michiel L. Petrus, Michiel Moes, Ruben D. Abellon, Pablo Docampo, and Tom J. Savenije. Charge transfer from methylammonium lead iodide perovskite to organic transport materials: Efficiencies, transfer rates, and interfacial recombination. *ADVANCED ENERGY MATERIALS*, 7(13), JUL 5 2017.

[45] Igal Levine, Satyajit Gupta, Achintya Bera, Davide Ceratti, Gary Hodes, David Cahen, Dengyang Guo, Tom J. Savenije, Jorge Avila, Henk J. Bolink, Oded Millo, Doron Azulay, and Isaac Balberg. Can we use time-resolved measurements to get steady-state transport data for halide perovskites? *JOURNAL OF APPLIED PHYSICS*, 124(10), SEP 14 2018.

[46] Tom J. Savenije, Dengyang Guo, Valentina M. Caselli, and Eline M. Hutter. Quantifying charge-carrier mobilities and recombination rates in metal halide perovskites from time-resolved microwave photoconductivity measurements. *ADVANCED ENERGY MATERIALS*, 10(26, SI), JUL 2020.

[47] Waqaas Rehman, Rebecca L. Milot, Giles E. Eperon, Christian Wehrenfennig, Jessica L. Boland, Henry J. Snaith, Michael B. Johnston, and Laura M. Herz. Charge-carrier dynamics and mobilities in formamidinium lead mixed-halide perovskites. *ADVANCED MATERIALS*, 27(48):7938–7944, DEC 22 2015.

[48] Zhaodong Chu, Chun-Yuan Wang, Jiamin Quan, Chenhui Zhang, Chao Lei, Ali Han, Xuejian Ma, Hao-Ling Tang, Dishan Abeysinghe, Matthew Staab, Xixiang Zhang, Allan H. MacDonald, Vincent Tung, Xiaoqin Li, Chih-Kang Shih, and Keji Lai. Unveiling defect-mediated carrier dynamics in monolayer semiconductors by spatiotemporal microwave. *PROCEEDINGS OF THE NATIONAL ACADEMY OF SCIENCES OF THE UNITED STATES OF AMERICA*, 117(25):13908–13913, JUN 23 2020.

[49] Giles E. Eperon, Samuel D. Stranks, Christopher Menelaou, Michael B. Johnston, Laura M. Herz, and Henry J. Snaith. Formamidinium lead trihalide: a broadly tunable perovskite for efficient planar heterojunction solar cells. *ENERGY & ENVIRONMENTAL SCIENCE*, 7(3):982–988, MAR 2014.

[50] Jin-Wook Lee, Deok-Hwan Kim, Hui-Seon Kim, Seung-Woo Seo, Sung Min Cho, and Nam-Gyu Park. Formamidinium and cesium hybridization for photo- and moisture-stable perovskite solar cell. *ADVANCED ENERGY MATERIALS*, 5(20, SI), OCT 21 2015.

[51] Chenyi Yi, Jingshan Luo, Simone Meloni, Ariadni Boziki, Negar Ashari-Astani, Carole Graetzel, Shaik M. Zakeeruddin, Ursula Roethlisberger, and Michael Graetzel. Entropic stabilization of mixed a-cation ABX(3) metal halide perovskites for high performance perovskite solar cells. *ENERGY & ENVIRONMENTAL SCIENCE*, 9(2):656–662, 2016.

[52] Michael Saliba, Taisuke Matsui, Ji-Youn Seo, Konrad Domanski, Juan-Pablo Correa-Baena, Mohammad Khaja Nazeeruddin, Shaik M. Zakeeruddin, Wolfgang Tress, Antonio Abate, Anders Hagfeldt, and Michael Gratzel. Cesium-containing triple cation perovskite solar cells: improved stability, reproducibility and high efficiency. *ENERGY & ENVIRONMENTAL SCIENCE*, 9(6):1989–1997, 2016.

[53] Zhen Li, Mengjin Yang, Ji-Sang Park, Su-Huai Wei, Joseph J. Berry, and Kai Zhu. Stabilizing perovskite structures by tuning tolerance factor: Formation of formamidinium and cesium lead iodide solid-state alloys. *CHEMISTRY OF MATERIALS*, 28(1):284–292, JAN 12 2016.

[54] Zhaodong Chu, Mengjin Yang, Philip Schulz, Di Wu, Xin Ma, Edward Seifert, Liuyang Sun, Xiaoqin Li, Kai Zhu, and Keji Lai. Impact of grain boundaries on efficiency and stability of organic-inorganic trihalide perovskites. *NATURE COMMUNICATIONS*, 8, DEC 20 2017.

[55] Zhaodong Chu, Ali Han, Chao Lei, Sergei Lopatin, Peng Li, David Wannlund, Di Wu, Kevin Herrera, Xixiang Zhang, Allan H. MacDonald, Xiaoqin Li, Lain-Jong Li, and Keji Lai. Energy-resolved photoconductivity mapping in a monolayer-bilayer WSe2 lateral heterostructure. *NANO LETTERS*, 18(11):7200–7206, NOV 2018.

[56] K. Lai, W. Kundhikanjana, M. Kelly, and Z. X. Shen. Modeling and characterization of a cantilever-based near-field scanning microwave impedance microscope. *REVIEW OF SCIENTIFIC INSTRUMENTS*, 79(6), JUN 2008.

[57] Toshiaki Kato and Toshiro Kaneko. Transport dynamics of neutral excitons and trions in monolayer WS2. *ACS NANO*, 10(10):9687–9694, OCT 2016.

[58] F. Cadiz, C. Robert, E. Courtade, M. Manca, L. Martinelli, T. Taniguchi, K. Watanabe, T. Amand, A. C. H. Rowe, D. Paget, B. Urbaszek, and X. Marie. Exciton diffusion in WSe2 monolayers embedded in a van der waals heterostructure. *APPLIED PHYSICS LETTERS*, 112(15), APR 9 2018.

[59] Jingfeng Song, Yuanyuan Zhou, Nitin P. Padture, and Bryan D. Huey. Anomalous 3d nanoscale photoconduction in hybrid perovskite semiconductors revealed by tomographic atomic force microscopy. *NATURE COMMUNICATIONS*, 11(1), JUL 3 2020.

[60] Esma Ugur, Jafar I. Khan, Erkan Aydin, Mingcong Wang, Mindaugas Kirkus, Marios Neophytou, Iain McCulloch, Stefaan De Wolf, and Frederic Laquai. Carrier extraction from perovskite to polymeric charge transport layers probed by ultrafast transient absorption spectroscopy. *JOURNAL OF PHYSICAL CHEMISTRY LETTERS*, 10(21):6921–6928, NOV 7 2019.

[61] Dehui Li, Hung-Chieh Cheng, Yiliu Wang, Zipeng Zhao, Gongming Wang, Hao Wu, Qiyuan He, Yu Huang, and Xiangfeng Duan. The effect of thermal annealing on charge transport in organolead halide perovskite microplate field-effect transistors. *ADVANCED MATERIALS*, 29(4), JAN 25 2017.

[62] Satyaprasad P. Senanayak, Bingyan Yang, Tudor H. Thomas, Nadja Giesbrecht, Wenchao Huang, Eliot Gann, Bhaskaran Nair, Karl Goedel, Suchi Guha, Xavier Moya, Christopher R. McNeill, Pablo Docampo, Aditya Sadhanala, Richard H. Friend, and Henning Sirringhaus. Understanding charge transport in lead iodide perovskite thin-film field-effect transistors. *SCIENCE ADVANCES*, 3(1), JAN 2017.

[63] Jae S. Yun, Anita Ho-Baillie, Shujuan Huang, Sang H. Woo, Yooun Heo, Jan Seidel, Fuzhi Huang, Yi-Bing Cheng, and Martin A. Green. Benefit of grain boundaries in organic-inorganic halide planar perovskite solar cells. *JOURNAL OF PHYSICAL CHEMISTRY LETTERS*, 6(5):875–880, MAR 5 2015.

[64] Da Seul Lee, Jae Sung Yun, Jincheol Kim, Arman Mahboubi Soufiani, Sheng Chen, Yongyoon Cho, Xiaofan Deng, Jan Seidel, Sean Lim, Shujuan Huang, and Anita W. Y. Ho-Baillie. Passivation of grain boundaries by phenethylammonium in formamidinium-methylammonium lead halide perovskite solar cells. *ACS ENERGY LETTERS*, 3(3):647–654, MAR 2018.

[65] Tejas S. Sherkar, Cristina Momblona, Lidon Gil-Escrig, Jorge Avila, Michele Sessolo, Henk J. Bolink, and L. Jan Anton Koster. Recombination in perovskite solar cells: Significance of grain boundaries, interface traps, and defect ions. *ACS ENERGY LETTERS*, 2(5):1214–1222, MAY 2017.

[66] Andres-Felipe Castro-Mendez, Juanita Hidalgo, and Juan-Pablo Correa-Baena. The role of grain boundaries in perovskite solar cells. *ADVANCED ENERGY MATERIALS*, 9(38), OCT 2019.

[67] Yuze Lin, Tao Li, Ye Liu, Behzad Bahrami, Dengyang Guo, Yanjun Fang, Yuchuan Shao, Ashraful Haider Chowdhury, Qi Wang, Yehao Deng, Alexei Gruverman, Tom J. Savenije, Qiquan Qiao, and Jinsong Huang. Perovskite solar cells with embedded homojunction via nonuniform metal ion doping. *CELL REPORTS PHYSICAL SCIENCE*, 2(5), MAY 19 2021.

[68] Yu Li, Weibo Yan, Yunlong Li, Shufeng Wang, Wei Wang, Zuqiang Bian, Lixin Xiao, and Qihuang Gong. Direct observation of long electron-hole diffusion

distance in CH3NH3PbI3 perovskite thin film. *SCIENTIFIC REPORTS*, 5, SEP 29 2015.

[69] Wenming Tian, Chunyi Zhao, Jing Leng, Rongrong Gui, and Shenge Jin. Visualizing carrier diffusion in individual single-crystal organolead halide perovskite nanowires and nanoplates. *JOURNAL OF THE AMERICAN CHEMICAL SOCIETY*, 137(39):12458–12461, OCT 7 2015.

[70] Makhsud Saidaminov, I, Kristopher Williams, Mingyang Wei, Andrew Johnston, Rafael Quintero-Bermudez, Maral Vafaie, Joao M. Pina, Andrew H. Proppe, Yi Hou, Grant Walters, Shana O. Kelley, William A. Tisdale, and Edward H. Sargent. Multi-cation perovskites prevent carrier reflection from grain surfaces. *NATURE MATERIALS*, 19(4):412+, APR 2020.

[71] Wan-Jian Yin, Tingting Shi, and Yanfa Yan. Unusual defect physics in CH3NH3PbI3 perovskite solar cell absorber. *APPLIED PHYSICS LETTERS*, 104(6), FEB 10 2014.

[72] Xie Zhang, Mark E. Turiansky, Jimmy-Xuan Shen, and Chris G. Van de Walle. Iodine interstitials as a cause of nonradiative recombination in hybrid perovskites. *PHYSICAL REVIEW B*, 101(14), APR 15 2020.

[73] Gang Wang, Alexey Chernikov, Mikhail M. Glazov, Tony F. Heinz, Xavier Marie, Thierry Amand, and Bernhard Urbaszek. Colloquium: Excitons in atomically thin transition metal dichalcogenides. *REVIEWS OF MODERN PHYSICS*, 90(2), APR 4 2018.

[74] Keliang He, Nardeep Kumar, Liang Zhao, Zefang Wang, Kin Fai Mak, Hui Zhao, and Jie Shan. Tightly bound excitons in monolayer WSe2. *PHYSICAL*

REVIEW LETTERS, 113(2), JUL 10 2014.

[75] Miguel M. Ugeda, Aaron J. Bradley, Su-Fei Shi, Felipe H. da Jornada, Yi Zhang, Diana Y. Qiu, Wei Ruan, Sung-Kwan Mo, Zahid Hussain, Zhi-Xun Shen, Feng Wang, Steven G. Louie, and Michael F. Crommie. Giant bandgap renormalization and excitonic effects in a monolayer transition metal dichalcogenide semiconductor. *NATURE MATERIALS*, 13(12):1091–1095, DEC 2014.

[76] Ziliang Ye, Ting Cao, Kevin O'Brien, Hanyu Zhu, Xiaobo Yin, Yuan Wang, Steven G. Louie, and Xiang Zhang. Probing excitonic dark states in single-layer tungsten disulphide. *NATURE*, 513(7517):214–218, SEP 11 2014.

[77] Emma C. Regan, Danqing Wang, Eunice Y. Paik, Yongxin Zeng, Long Zhang, Jihang Zhu, Allan H. MacDonald, Hui Deng, and Feng Wang. Emerging exciton physics in transition metal dichalcogenide heterobilayers. *NATURE REVIEWS MATERIALS*, 7(10):778–795, OCT 2022.

[78] Qing Hua Wang, Kourosh Kalantar-Zadeh, Andras Kis, Jonathan N. Coleman, and Michael S. Strano. Electronics and optoelectronics of two-dimensional transition metal dichalcogenides. *NATURE NANOTECHNOLOGY*, 7(11):699–712, NOV 2012.

[79] Di Huang, Junho Choi, Chih-Kang Shih, and Xiaoqin Li. Excitons in semiconductor moire superlattices. *NATURE NANOTECHNOLOGY*, 17(3):227–238, MAR 2022.

[80] Appu Paduthol, Mattias Klaus Juhl, and Thorsten Trupke. Addressing limitations of photoluminescence based external quantum efficiency measurements. *JOURNAL OF APPLIED PHYSICS*, 123(2), JAN 14 2018.

[81] Andrea Splendiani, Liang Sun, Yuanbo Zhang, Tianshu Li, Jonghwan Kim, Chi-Yung Chim, Giulia Galli, and Feng Wang. Emerging photoluminescence in monolayer MoS2. *NANO LETTERS*, 10(4):1271–1275, APR 2010.

[82] Aaron M. Jones, Hongyi Yu, Nirmal J. Ghimire, Sanfeng Wu, Grant Aivazian, Jason S. Ross, Bo Zhao, Jiaqiang Yan, David G. Mandrus, Di Xiao, Wang Yao, and Xiaodong Xu. Optical generation of excitonic valley coherence in monolayer wse2. *NATURE NANOTECHNOLOGY*, 8(9):634–638, SEP 2013.

[83] Alexey Chernikov, Timothy C. Berkelbach, Heather M. Hill, Albert Rigosi, Yilei Li, Ozgur Burak Aslan, David R. Reichman, Mark S. Hybertsen, and Tony F. Heinz. Exciton binding energy and nonhydrogenic rydberg series in monolayer WS2. *PHYSICAL REVIEW LETTERS*, 113(7), AUG 13 2014.

[84] Mathieu Massicotte, Fabien Vialla, Peter Schmidt, Mark B. Lundeberg, Simone Latini, Sten Haastrup, Mark Danovich, Diana Davydovskaya, Kenji Watanabe, Takashi Taniguchi, Vladimir I. Fal'ko, Kristian S. Thygesen, Thomas G. Pedersen, and Frank H. L. Koppens. Dissociation of two-dimensional excitons in monolayer WSe2. *NATURE COMMUNICATIONS*, 9, APR 24 2018.

[85] Jason S. Ross, Pasqual Rivera, John Schaibley, Eric Lee-Wong, Hongyi Yu, Takashi Taniguchi, Kenji Watanabe, Jiaqiang Yan, David Mandrus, David Cobden, Wang Yao, and Xiaodong Xu. Interlayer exciton optoelectronics in a 2d heterostructure p-n junction. *NANO LETTERS*, 17(2):638–643, FEB 2017.

[86] Daniel Vaquero, Vito Clerico, Juan Salvador-Sanchez, Adrian Martin-Ramos, Elena Diaz, Francisco Dominguez-Adame, Yahya M. Meziani, Enrique Diez, and Jorge Quereda. Excitons, trions and rydberg states in monolayer MoS2

revealed by low-temperature photocurrent spectroscopy. *COMMUNICATIONS PHYSICS*, 3(1), OCT 30 2020.

[87] Yuan Liu, Nathan O. Weiss, Xidong Duan, Hung-Chieh Cheng, Yu Huang, and Xiangfeng Duan. Van der waals heterostructures and devices. *NATURE REVIEWS MATERIALS*, 1(9), SEP 2016.

[88] Fabian Cadiz, Cedric Robert, Gang Wang, Wilson Kong, Xi Fan, Mark Blei, Delphine Lagarde, Maxime Gay, Marco Manca, Takashi Taniguchi, Kenji Watanabe, Thierry Amand, Xavier Marie, Pierre Renucci, Sefaattin Tongay, and Bernhard Urbaszek. Ultra-low power threshold for laser induced changes in optical properties of 2d molybdenum dichalcogenides. *2D MATERIALS*, 3(4), DEC 2016.

[89] Artur P. Herman, Szymon J. Zelewski, Kamil Misztal, and Robert Kudrawiec. Probing the long-lived photo-generated charge carriers in transition metal dichalcogenides by time-resolved microwave photoconductivity. *NANOPHOTONICS*, 11(7):1335–1344, APR 4 2022.

[90] Jeffrey L. Blackburu, Hanyu Zhang, Alexis R. Myers, Jeremy R. Dunklin, David C. Coffey, Rebecca N. Hirsch, Derek Vigil-Fowler, Seok Joon Yun, Byeong Wook Cho, Young Hee Lee, Elisa M. Miller, Garry Rumbles, and Obadiah G. Reid. Measuring photoexcited free charge carriers in mono- to few-layer transition-metal dichalcogenides with steady-state microwave conductivity. *JOURNAL OF PHYSICAL CHEMISTRY LETTERS*, 11(1):99–107, JAN 2 2020.

[91] Peng Chen, Timothy L. Atallah, Zhaoyang Lin, Peiqi Wang, Sung-Joon Lee, Junqing Xu, Zhihong Huang, Xidong Duan, Yuan Ping, Yu Huang, Justin R.

Caram, and Xiangfeng Duan. Approaching the intrinsic exciton physics limit in two-dimensional semiconductor diodes. *NATURE*, 599(7885):404+, NOV 18 2021.

[92] F URBACH. The long-wavelength edge of photographic sensitivity and of the electronic absorption of solids. *PHYSICAL REVIEW*, 92(5):1324, 1953.

[93] Thomas Mueller and Ermin Malic. Exciton physics and device application of two-dimensional transition metal dichalcogenide semiconductors. *NPJ 2D MATERIALS AND APPLICATIONS*, 2, SEP 10 2018.

[94] Kin Fai Mak, Keliang He, Jie Shan, and Tony F. Heinz. Control of valley polarization in monolayer MoS2 by optical helicity. *NATURE NANOTECHNOLOGY*, 7(8):494–498, AUG 2012.

[95] Xiao-Xiao Zhang, Ting Cao, Zhengguang Lu, Yu-Chuan Lin, Fan Zhang, Ying Wang, Zhiqiang Li, James C. Hone, Joshua A. Robinson, Dmitry Smirnov, Steven G. Louie, and Tony F. Heinz. Magnetic brightening and control of dark excitons in monolayer WSe2. *NATURE NANOTECHNOLOGY*, 12(9):883+, SEP 2017.

[96] Wu Zhou, Xiaolong Zou, Sina Najmaei, Zheng Liu, Yumeng Shi, Jing Kong, Jun Lou, Pulickel M. Ajayan, Boris I. Yakobson, and Juan-Carlos Idrobo. Intrinsic structural defects in monolayer molybdenum disulfide. *NANO LETTERS*, 13(6):2615–2622, JUN 2013.

[97] Hogni C. Kamban and Thomas G. Pedersen. Field-induced dissociation of two-dimensional excitons in transition metal dichalcogenides. *PHYSICAL REVIEW B*, 100(4), JUL 17 2019.

[98] K. Lai, W. Kundhikanjana, M. Kelly, and Z. X. Shen. Modeling and characterization of a cantilever-based near-field scanning microwave impedance microscope. *REVIEW OF SCIENTIFIC INSTRUMENTS*, 79(6), JUN 2008.

[99] Alejandro Molina-Sanchez, Maurizia Palummo, Andrea Marini, and Ludger Wirtz. Temperature-dependent excitonic effects in the optical properties of single-layer MoS2. *PHYSICAL REVIEW B*, 93(15), APR 26 2016.

[100] Sefaattin Tongay, Jian Zhou, Can Ataca, Kelvin Lo, Tyler S. Matthews, Jingbo Li, Jeffrey C. Grossman, and Junqiao Wu. Thermally driven crossover from indirect toward direct bandgap in 2d semiconductors: MoSe2 versus MoS2. *NANO LETTERS*, 12(11):5576–5580, NOV 2012.

[101] T. Korn, S. Heydrich, M. Hirmer, J. Schmutzler, and C. Schueller. Low-temperature photocarrier dynamics in monolayer MoS2. *APPLIED PHYSICS LETTERS*, 99(10), SEP 5 2011.

[102] G. Plechinger, F. X. Schrettenbrunner, J. Eroms, D. Weiss, C. Schueller, and T. Korn. Low-temperature photoluminescence of oxide-covered single-layer MoS2. *PHYSICA STATUS SOLIDI-RAPID RESEARCH LETTERS*, 6(3):126–128, MAR 2012.

[103] Jason S. Ross, Sanfeng Wu, Hongyi Yu, Nirmal J. Ghimire, Aaron M. Jones, Grant Aivazian, Jiaqiang Yan, David G. Mandrus, Di Xiao, Wang Yao, and Xiaodong Xu. Electrical control of neutral and charged excitons in a monolayer semiconductor. *NATURE COMMUNICATIONS*, 4, FEB 2013.

[104] Igor Vaskivskyi, Jan Gospodaric, Serguei Brazovskii, Damjan Svetin, Petra Sutar, Evgeny Goreshnik, Ian A. Mihailovic, Tomaz Mertelj, and Dragan Mi-

hailovic. Controlling the metal-to-insulator relaxation of the metastable hidden quantum state in 1T-TaS2. *SCIENCE ADVANCES*, 1(6), JUL 2015.

[105] L. Stojchevska, I. Vaskivskyi, T. Mertelj, P. Kusar, D. Svetin, S. Brazovskii, and D. Mihailovic. Ultrafast switching to a stable hidden quantum state in an electronic crystal. *SCIENCE*, 344(6180):177–180, APR 11 2014.

[106] Katsumi Tanimura. Photoinduced discommensuration of the commensurate charge-density wave phase in 1T-TaS2. *PHYSICAL REVIEW B*, 97(24), JUN 11 2018.